

Classifier-Free Guidance: From High-Dimensional Analysis to Generalized Guidance Forms

Krunoslav Lehman Pavasovic^{1,2}, Jakob Verbeek¹, Giulio Biroli^{2,†}, Marc Mezard^{3,†}

¹FAIR at Meta, ²École Normale Supérieure, Paris, ³Bocconi University, Milan

[†]Joint last author

Classifier-Free Guidance (CFG) is a widely adopted technique in diffusion and flow-based generative models, enabling high-quality conditional generation. A key theoretical challenge is characterizing the distribution induced by CFG, particularly in high-dimensional settings relevant to real-world data. Previous works have shown that CFG modifies the target distribution, steering it towards a distribution sharper than the target one, more shifted towards the boundary of the class. In this work, we provide a high-dimensional analysis of CFG, showing that these distortions vanish as the data dimension grows. We present a “blessing-of-dimensionality” result demonstrating that in sufficiently high and infinite dimensions, CFG accurately reproduces the target distribution. Using our high-dimensional theory, we show that there is a large family of guidances enjoying this property, in particular non-linear CFG generalizations. We study a simple non-linear “power-law” version, for which we demonstrate improved robustness, sample fidelity and diversity. Our findings are validated with experiments on class-conditional and text-to-image generation using state-of-the-art diffusion and flow-matching models.

Date: May 23, 2025

Correspondence: Krunoslav Lehman Pavasovic at krunolp@meta.com



Figure 1 Qualitative comparison of unguided sampling, standard Classifier-Free Guidance (CFG), and our proposed non-linear power-law version (DiT/XL-2 on ImageNet-1K 256×256). Standard CFG increases fidelity at a substantial expense to diversity and semantic meaning compared to unguided CFG. Our power-law guidance improves fidelity at no cost to semantics or diversity. Samples in each column start from the same seed.

1 Introduction

Diffusion (Sohl-Dickstein et al., 2015; Song and Ermon, 2020; Ho et al., 2020) and flow-based methods (Lipman et al., 2022; Albergo et al., 2023; Liu et al., 2022) have emerged as the de facto state-of-the-art for generating high-dimensional signals such as images, video, audio and molecular structures. Diffusion relies

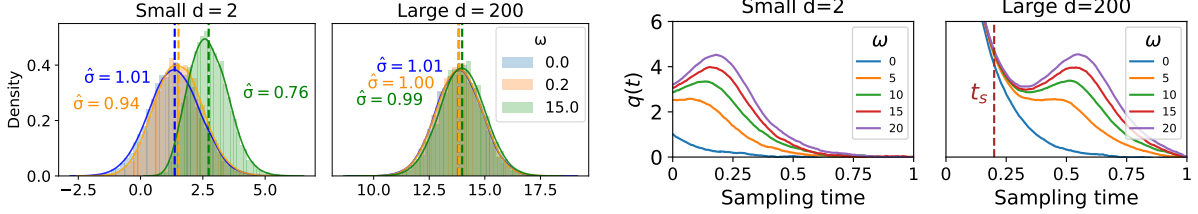


Figure 2 Left: CFG produces the exact target distribution in high dimensions. We simulate the backward process using a two Gaussian mixture. We project and plot the generated samples onto the target mean $+\vec{m}$: $q(t=0) = \vec{x} \cdot \vec{m}/|\vec{m}|$. For small $d = 2$, CFG generates a distribution with larger magnitude mean (dashed line) and smaller variance than the target one (for $\omega = 0$). This effect diminishes as the dimension increases: for $d = 200$ it is practically absent. **Right: High-dimensionality of the data allows CFG trajectories to align.** We plot the evolution of the mean of trajectories $q(t)$: starting at large forward times denoted with $t = 1$ (noise), for small $d = 2$, CFG trajectories do not align with the unconditional trajectories at $t = 0$ (data) causing the CFG overshoot. For large dimension $d = 200$, the high-dimensionality of the data allows trajectories to realign with the unguided one at speciation time t_s , resulting in the correct target distribution.

on Orstein-Uhlenbeck Langevin dynamics, where noise is progressively added to the data until it becomes completely random. New samples are generated by reversing this process through a time-reversed Langevin equation. This backward evolution is steered by a force, the *score*, estimated from the data. In contrast, flow matching circumvents the diffusion construction by directly specifying the probability paths between noise and data. This is done by regressing onto a target vector field which in turn generates the desired probability paths. An important task for both paradigms is generating data conditioned on a class label or textual description of the image content. This can be achieved through conditioning mechanisms in the model architecture, as well as guidance techniques (Dhariwal and Nichol, 2021; Ho and Salimans, 2022) that steer the generation process towards samples aligned with user intentions or desired properties.

The notion of guidance was first introduced in classifier guidance (Song et al., 2020a; Dhariwal and Nichol, 2021), where a pre-trained classifier is leveraged to induce class conditioning of the sampling. Although beneficial, relying on a pre-trained classifier can be computationally expensive and may introduce biases inherent to the classifier itself. Classifier-free guidance (CFG) (Ho and Salimans, 2022) was developed as an alternative, and was quickly adopted as a standard technique in state-of-the-art generative models (Nichol et al., 2021; Betker et al., 2023; Saharia et al., 2022; Esser et al., 2024). CFG does not rely on an auxiliary classifier, instead, the model is trained to generate unconditional and conditional samples, and at inference extrapolates the denoising path towards the conditional one. Using CFG, however, *it is no longer guaranteed* to sample the original conditional distribution. Indeed, CFG modifies it by steering it towards a “mode” of high-quality and input-consistent samples, while reducing sample diversity in the process (Astolfi et al., 2024).

The effectiveness of CFG remains surprising in many ways, and a main theoretical question is to characterize the distributions generated by CFG and how they compare to the target distribution. Recent theoretical works on CFG formally showed that in case of Gaussian mixtures in one and finite dimensions, it results in a sharper distribution than the target one, and more shifted towards the boundary of the class (Chidambaram et al., 2024; Xia et al., 2024; Wu et al., 2024; Bradley and Nakkiran, 2024). This effect, which is exemplified in Figure 2 for a two-dimensional Gaussian mixture, is similar to what found by practitioners, see *e.g.*, Saharia et al. (2022). From the theoretical point of view, it is important to analyze cases in which data is very high-dimensional, as in real applications, to assess also in this context the properties of the distributions generated by CFG, and how they compare to the target one. In this study, we address these questions developing a high-dimensional analysis of CFG, and use our high-dimensional results as guidelines to further enhance CFG’s practical application.

In summary, our contributions are two-fold:

- (1). We theoretically describe CFG’s behavior in high and infinite dimensions. We precisely characterize how increasing dimension affects mean overshoot and variance shrinkage. By linking CFG to the emergence of dynamical regimes (Biroli et al., 2024), we show that in sufficiently high dimensions, CFG-guided paths realign with those of the unguided conditional path that generates the unmodified distribution. Therefore, CFG can indeed generate the target distribution, and its role is to accelerate sample convergence to the desired class. This path alignment coincides precisely with the symmetry-breaking and class formation (Biroli and

Mézard, 2023; Raya and Ambrogioni, 2024). We demonstrate our theory aligns with numerical simulations and state-of-the-art diffusion and flow-matching experiments (Sadat et al., 2023; Sehwag et al., 2022).

(2). Using our developed theory, we put forward a family of guidance strategies generalizing CFG. We experimentally demonstrate their desirable properties: reduced overshoot, dampened variance shrinkage and faster convergence to the target distribution. We apply these to state-of-the-art diffusion and flow matching models, showcasing improved sample quality, consistency, and diversity.

2 Related work

Introducing CFG, Ho and Salimans (2022) highlighted the trade-off between image quality, measured by Fréchet inception distance (FID, Heusel et al. (2017)), and diversity, measured by inception score (Salimans et al., 2016) when adjusting the guidance strength parameter ω . Since then, a significant body of research has examined CFG from various perspectives.

Theoretical works on CFG. Several works employed Gaussian mixture models (GMMs) to analyze diffusion and guidance, including Shah et al. (2023); Liang et al. (2024); Cui et al. (2023); Bai et al. (2024); Song et al. (2020a). In contrast, Du et al. (2023) explored alternative conditioning, while Bradley and Nakkiran (2024) characterized CFG as a predictor-corrector (Song et al., 2020a). Most relevant to this work, Chidambaram et al. (2024) demonstrated CFG’s mean overshoot and variance shrinkage in one-dimensional settings, while Wu et al. (2024) extended the findings to multi-dimensions using GMMs. We expand on these by developing a high-dimensional statistical analysis and precisely characterizing how these effects diminish as dimensionality increases, ultimately demonstrating that the CFG-generated distribution in fact aligns with the target one for $d \rightarrow \infty$.

CFG variants and experimental analyses. Among experimental analyses of CFG, Karras et al. (2024a) propose guiding generation using a less-trained version of the model, Kynkäänniemi et al. (2024) apply CFG during a limited interval, and Wang et al. (2024) use weight schedulers for the classifier strength parameter. Several other CFG alternatives have been proposed, such as rectified guidance (Xia et al., 2024), projected score guidance (Kadkhodaie et al., 2024), characteristic guidance (Zheng and Lan, 2023), second-order CFG (Sun et al., 2023), CADs (Sadat et al., 2023), CFG++ (Chung et al., 2024), REG (Xia et al., 2024) and APG (Sadat et al., 2024). In later sections, we demonstrate our framework generalizes to these variants, consistently enhancing performance.

Dynamical regimes, statistical physics and high-dimensional settings. Statistical physics methods have shown particularly useful in analyzing high-dimensional generative models, *e.g.*, data from Curie-Weiss models (Biroli and Mézard, 2023), high-dimensional Gaussian mixtures (Biroli et al., 2024), and hierarchical models (Sclocchi et al., 2024). Furthermore, several recent works studied dynamical regimes diffusion models (Biroli and Mézard, 2023; Raya and Ambrogioni, 2024; Biroli et al., 2024; Sclocchi et al., 2024; Yu and Huang, 2024; Li and Chen, 2024; Aranguri et al., 2025), however none of them analyzed the effects brought by classifier-free guidance.

3 Background and high-level discussion

We begin by providing an overview of the standard framework for generative diffusion, serving as the foundation for our analysis¹. We let $\{\vec{a}_i\}_{i=1}^n \in \mathbb{R}^d$ represent n independent data points sampled from the *true* underlying data distribution $P_0(\vec{a})$ that we aim to model.

¹For clarity of presentation, our exposition focuses on diffusion, though our findings directly extend to flow-matching with Gaussian paths, as discussed in Sec. 4.10.2 of Lipman et al. (2024).

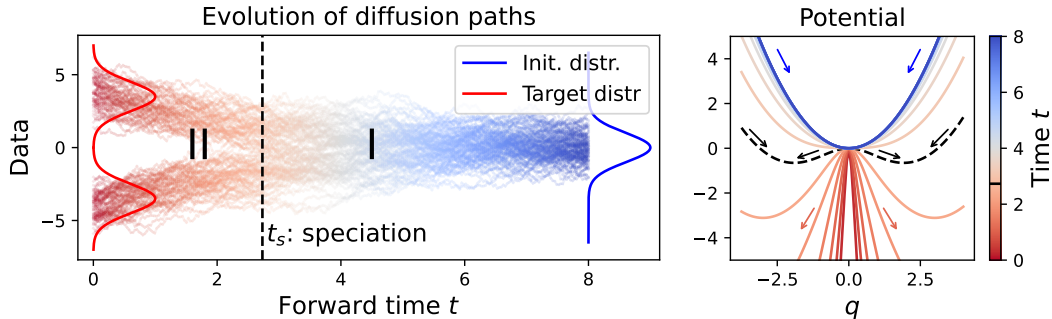


Figure 3 Dynamical regimes in diffusion. **Left:** Illustration of the speciation phenomenon using a one-dimensional Gaussian mixture. Starting from pure Gaussian noise at large time t , the backward diffusion begins in Regime I, where the class has not been decided yet. After speciation time t_s (dashed line), the class membership is decided. **Right:** Evolution of the effective potential (conditional potential in Eq. (6)) over time for high-dimensional Gaussian mixture showcasing the symmetry breaking phenomenon.

3.1 General setup

The forward diffusion process, starting from the data points $\{\vec{a}_i\}_{i=1}^n$, is modeled by an Ornstein-Uhlenbeck process, described by the following stochastic differential equation (SDE):

$$d\vec{x}(t) = -\vec{x}(t) dt + \sqrt{2} d\vec{B}(t), \quad (1)$$

where $d\vec{B}(t)$ denotes the standard Brownian motion in \mathbb{R}^d . At any given time t , the state $\vec{x}(t)$ is distributed according to a Gaussian with mean $\vec{a}e^{-t}$ and variance $\Delta_t = 1 - e^{-2t}$. The forward process is terminated at time $t_f \gg 1$, when $\vec{x}(t_f)$ is effectively pure Gaussian noise, distributed as $\mathcal{N}(0, \mathcal{I}_d)$, with \mathcal{I}_d being the identity matrix in \mathbb{R}^d .

The backward diffusion process operates in reverse time $\tau = t_f - t$, described by the following SDE:

$$d\vec{x}(\tau) = \vec{x}(\tau) d\tau + 2\vec{S}(\vec{x}, \tau) d\tau + \sqrt{2} d\vec{B}(\tau), \quad (2)$$

where $\vec{S}(\vec{x}, t) = \vec{\nabla} \log P_t(\vec{x})$ denotes the score function. The backward diffusion process generates points \vec{x} sampled from the distribution $P_t(\vec{x})$ for every time step τ . At the end of the backward process, *i.e.*, when $\tau = 0$, the process generates points drawn from the original distribution P_0 .

In this work, we focus on generating data that can be categorized into distinct classes. We begin by assuming that the underlying data distribution is a d -dimensional probability distribution $P_0(\vec{x}, c)$, where c represents a discrete class index and \vec{x} a d -dimensional vector. The aim is to generate data conditioned on c , the class label. The procedure that is mathematically guaranteed to generate the exact conditional target distribution consists of using the true conditional score, $\vec{S}_t(\vec{x}, c) = \vec{\nabla} \log P_t(\vec{x}|c)$ in Eq. (2). CFG, however, does not do that; it instead further directs diffusion in a manner proportional to the difference between conditional and unconditional scores:

$$S_t^{\text{CFG}}(\vec{x}, c) = S_t(\vec{x}, c) + \omega[S_t(\vec{x}, c) - S_t(\vec{x})]. \quad (3)$$

Although CFG may offer practical advantages, such as enhanced fidelity and classification confidence (Wu et al., 2024), a key question remains: whether CFG is at all capable of accurately generating the desired target distribution.

3.2 Connecting dynamical regimes of diffusion to classifier-free guidance

Our analysis adopts the approach outlined by Biroli and Mézard (2023) and Biroli et al. (2024), which identifies three distinct regimes: our exposition focuses on the first two, as the effect of CFG is the same in the second and third one. The first two regimes are distinguished by symmetry-breaking, characterized through the eigenvalue of the principal component of the data covariance matrix.

CFG and distinct dynamical regimes. Biroli et al. (2024) analyze the dynamical regimes of the backward process in Eq. (2) for two classes with $d \rightarrow \infty$. They identify *speciation time* t_s as the transition between the first and second regime. In Regime I, the backward trajectories have not yet committed to a particular class of data. In Regime II, the trajectories have committed to a class and generate the features necessary to produce samples from that class. As exemplified in Figure 3, in Regime II, the probability $P_t(\vec{x})$ consists of separated non-overlapping lumps corresponding to the target classes.

In our work, we show that CFG is beneficial in Regime I as the class membership of the trajectories has not been decided yet, whereas in Regime II the well-separated probability lumps corresponding to different classes make CFG redundant. This can be stated as three results:

Result I. Before speciation time t_s , CFG is effective in aiding class selection and speeds up the convergence towards the target class.

Result II. Just before speciation time t_s , CFG-guided paths realign with the unguided path that generates the correct, unmodified target distribution.

Result III. After speciation time t_s , CFG has no effect on the generation process.

In Section 4, we substantiate these results with theoretical arguments for the case of Gaussian mixtures, showing first that for $d \rightarrow \infty$ CFG reproduces the correct target distributions, and then characterizing the finite- d corrections. In Section 5 we then demonstrate their applicability to enhance performance of real-world models.

4 CFG in the high-dimensional limit of Gaussian mixtures

Distinct dynamical regimes emerge in a wide range of generative models and across various data modalities (Ventura et al., 2024; George et al., 2025; Bae et al., 2024). To examine the dynamical regimes, we adopt the two-Gaussian mixture framework of Biroli and Mézard (2023), which has been tested on real data and shown to hold for models of data lying on manifolds (Biroli et al., 2024)².

4.1 Theoretical framework

We examine the case where $P_0(\vec{a})$ is a superposition of two Gaussians with equal weight, means $\pm\vec{m}$ and isotropic variance σ^2 . To ensure the two Gaussians are well separated, we take the large d limit with fixed values of $|\vec{m}|^2/d$ and σ . We assume that the exact scores are available.

In this setting, the speciation transition between Regimes I and II resembles a symmetry-breaking phenomenon occurring on timescales $t_s = \frac{1}{2} \log(d)$. Biroli et al. (2024) show t_s emerges as the time at which diffusion paths commit to a specific class by relating it to a change of the potential in the backward Langevin equation, as displayed in Figure 3. We find that *the speciation time t_s aligns precisely with the time until which CFG is effective in aiding class selection.* Beyond this point, as the trajectories have committed to a class, CFG no longer influences the generated outcome. We now spell out the required theoretical arguments, with detailed proofs presented in App. B and App. C.

4.2 Key findings: Infinite dimensional limit

We first rewrite the distribution of \vec{x} at time t as $P_t(\vec{x}) \propto [e^{-(\vec{x}-\vec{m}e^{-t})^2/(2\Gamma_t)} + e^{-(\vec{x}+\vec{m}e^{-t})^2/(2\Gamma_t)}]$, where $\Gamma_t = 1 + (\sigma^2 - 1)e^{-2t}$. In this case, the CFG formula in Eq. (3) can be rewritten as:

$$S_t^{\text{CFG}}(\vec{x}, c) = -\frac{\vec{x}}{\Gamma_t} + \frac{c\vec{m}e^t}{\Gamma_t} + \omega \frac{\vec{m}e^{-t}}{\Gamma_t} \left\{ c - \tanh\left(\frac{\vec{x} \cdot \vec{m}e^{-t}}{\Gamma_t}\right) \right\}, \quad (4)$$

with $c = \pm 1$ and $\omega > 0$.

²Our analysis can be extended to any number of Gaussians, with different variances, or data supported on manifolds, by following e.g., Achilli et al. (2025); George et al. (2025). We provide discussion in App. C.

Result I: Before speciation time t_s , CFG is effective in aiding class selection and speeds up the convergence towards the target class. To obtain this result, we examine $S_t^{\text{CFG}}(\vec{x}, c)$ (4) in Regime I, which lasts until speciation occurs at $t_s = (1/2) \log d$.

Which directions of Eq. (4) are affected by CFG? Eq. (4) shows that CFG only affects the \vec{m} directions (as it is the direction multiplied by ω), therefore CFG has no effect on orthogonal directions $\vec{v} \perp \vec{m}$. This is formally shown by projecting the backward Eq. (2) on a unit vector orthogonal to \vec{m} : the resulting equation $dp = p(1 - 2/\Gamma_{t_f - \tau})d\tau + \sqrt{2}dB$ equals the backward equation for an initial Gaussian $\mathcal{N}(0, \sigma^2)$, thus not depending on ω and therefore unaffected by CFG.

What happens in the \vec{m} directions? As CFG only affects \vec{m} directions in Eq. (4), let us project onto \vec{m} and observe how the CFG score S_t^{CFG} influences the backward process. Defining $q(t) := \frac{\vec{x} \cdot \vec{m}}{|\vec{m}|}$ where $|\vec{m}| = \sqrt{d}$, the evolution guided to class $c = 1$ is given by the following:

$$dq = \left(q + 2 \left[-q + e^{-(t_f - t_s - \tau)} \left((1 + \omega) - \omega \tanh \left(q e^{-(t_f - t_s - \tau)} \right) \right) \right] \right) d\tau + d\eta(\tau), \quad (5)$$

where $\tau = t_f - t$, with $t_s = (1/2) \log d$. Here, $\eta(\tau)$ denotes $\sqrt{2}$ times a Brownian motion, and we used the fact that in Regime I we have $\Gamma_t \simeq 1$, see Biroli et al. (2024). To simplify notation, we omit the dependency $t(\tau)$ for backward time and use t hereafter.

By rewriting Eq. (5) as: $dq = -\frac{\partial V^{\text{CFG}}(q, \tau)}{\partial q} d\tau + d\eta(\tau)$, we can analyze the effective potential:

$$V^{\text{CFG}} = \underbrace{\left(\frac{1}{2} q^2 - 2e^{-(t-t_s)} q \right)}_{\text{Conditional potential}} + \omega \underbrace{\left[-q e^{-(t-t_s)} + \ln \cosh \left(q e^{-(t-t_s)} \right) \right]}_{\text{Extra CFG potential } V_{\text{extra}}}. \quad (6)$$

Result I follows from Eq. (6): we observe that CFG-added-potential provides an additional push toward the positive values of q , corresponding to target class $c = 1$. The effect of CFG is particularly strong for trajectories deviating from typical behavior: its effect is particularly prominent when correcting the trajectories going toward the wrong class (see Figure 7 in App. B).

Result II: CFG paths align before exiting Regime I. During late stage of Regime I, q becomes of order \sqrt{d} (Biroli and Mézard, 2023), while the CFG-added-term in Eq. (4) gives exponentially small corrections to the SDE. At these late times τ_i of Reg. I, SDE Eq. (4) simplifies to: $dq = -q + 2e^{-(t_f - t_s - \tau_i)} + d\eta(\tau_i)$. Although different values of ω have led to different values of $q(\tau_i)$ during the backward process, we show that the value $q(\tau_i)$ is exponentially quickly forgotten when τ departs from τ_i . Therefore, the backward evolution readjusts to the “correct” value without CFG.

Result II is therefore obtained by solving the SDE starting from τ_i : $q(\tau) = q(\tau_i) e^{-(\tau - \tau_i)} + e^{-(t_f - t_s)} (e^\tau - e^{-\tau + 2\tau_i}) + \sqrt{1 - e^{-(2(\tau - \tau_i))}} z_\tau$, where z_τ denotes a standard Gaussian variable. When $\tau \gg \tau_i$ but still in Regime I, the solution of the SDE does not depend any longer on $q(\tau_i)$ and it coincides statistically with the one of the backward process of the single Gaussian corresponding to the target class $c = +1$.

Result III: After speciation time t_s , CFG has no effect on the generation process. At the end of Regime I, q diverges so one has to focus on the rescaled variable $\vec{x} \cdot \vec{m}/d$. As q has realigned with the value it would have had without CFG (for $\omega = 0$), the initial condition ($\vec{x} \cdot \vec{m}/d = 0$) in Regime II is independent of ω . To see that CFG has no effect in this regime, all that is left to show is that the term CFG-added term (multiplied by ω) in Eq. (4) is zero. From Biroli et al. (2024) we know that in Regime II, $|\vec{x} \cdot \vec{m}| e^{-t}/\Gamma_t$ is of order $O(d)$ and $\text{sign}(\vec{x} \cdot \vec{m}) = 1$. Thus, Result III follows by observing the extra CFG term in Eq. (4) thus equals zero as $1 - \tanh(\vec{x} \cdot \vec{m} e^{-t}/\Gamma_t) \rightarrow 0$ for $d \rightarrow \infty$.

To summarize during Regime I, CFG pushes faster towards the target distribution. Before speciation t_s occurs, the paths realign with the correct, unguided path. Once Regime II kicks in, CFG no longer affects the generation process. This can be observed in Figure 2 (right), where Eq. (5) is simulated for $t_s = 1000, \sigma = 1$, averaging over 10,000 trajectories. This shows that, unlike in low-dimensions where the paths never realign

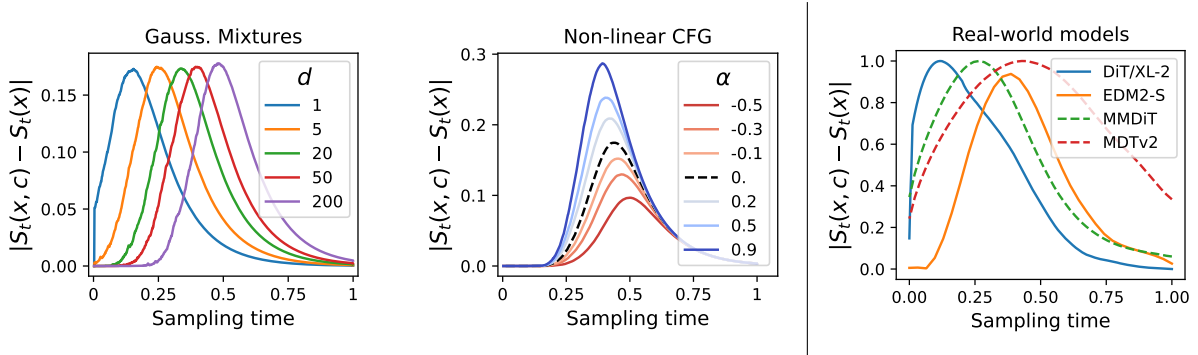


Figure 4 Evolution of the CFG score difference, from noise ($t = 1$) to data ($t = 0$). **Left (stand. CFG):** Numerically simulating mixture of two Gaussians: as d increases, the score difference becomes substantial earlier (this happens during Regime I). **Middle (non-lin. CFG, $d = 200$):** Non-linear CFG parameter α allows more flexible behavior of the score difference. **Right (stand. CFG):** Real-world experiments using advanced models show consistent behavior with theory: monotonically increasing score difference followed by decay after a certain point. Experimental details are provided in App. E and F.

(see, e.g., Chidambaram et al. (2024)), large dimensionality of the data allows CFG to indeed generate the correct target distribution, as seen in Figure 2 (left).

4.3 Key findings: Finite dimensional setting

So far, we have shown that for any value of ω the target distribution is correctly reproduced in the infinite- d limit. We now consider the changes brought by finite d .

Consistent conclusions in large, finite d . Within Regime I, for large, yet finite dimension, the CFG-added-term in the score in Eq. (4) remains of the same order as the conditional score of the unguided path so CFG has the same effect as in the infinite limit. When exiting Regime I and during Regime II, the extra CFG term is zero for $d \rightarrow \infty$, and exponentially small in d for finite d , so the remaining two results carry over as well.

Mean overshoot and variance shrinkage in small d . In low dimensions, the paths will not realign when exiting Regime I. The additional push introduced by CFG within Regime I will have an effect on Regime II, resulting in an overshoot of the target distribution of relative amplitude of order $1/\sqrt{d}$. The CFG-added-term also results in a larger second derivative of the potential $V^{\text{CFG}}(q, t)$. Thus, the resulting CFG Langevin equation is associated to a more confining potential, ultimately shrinking the variance of the CFG-generated distribution. These are in line with previous empirical (Ho and Salimans, 2022) and theoretical findings (Chidambaram et al., 2024; Wu et al., 2024).

So far, we have shown that CFG correctly generates the target distribution in infinite dimensions and modifies in lower dimensions in a way that is consistent from low dimensions to large dimensions (Chidambaram et al., 2024; Wu et al., 2024). These theoretical results support the use of CFG in practical applications, by establishing general properties of the CFG-generated distributions. This raises the question: can we use the high-dimensional results as a guideline to design guidance schemes that enjoy similar properties of standard CFG, and in particular preserve the same behavior in high and infinite dimensions? In the next section, we provide an affirmative answer and present new CFG-procedures.

5 Generalized classifier-free guidance

The “blessing of dimensionality” that allows CFG to generate the target distribution in high-dimensions is due to two main properties: (1) CFG acts in Regime I pushing stronger toward the desired class, (2) CFG does not play any role in Regime II where the detailed properties of the data are generated. There is, however, a larger class of guidance schemes that also enjoy these properties. As a straightforward but effective extension, we introduce non-linear variants of CFG.

5.1 Non-linear classifier-free guidance

We consider non-linear versions of score-based guidance of the form:

$$S_t^{\text{CFG-NL}}(\vec{x}, c) = S_t(\vec{x}, c) + [S_t(\vec{x}, c) - S_t(\vec{x})] \phi_t \left(\left| \vec{S}_t(\vec{x}, c) - \vec{S}_t(\vec{x}) \right| \right). \quad (7)$$

For constant $\phi_t(s) = \omega$, Eq. (7) reduces to standard CFG. As long as the function $\phi_t(s)$ satisfies $\lim_{s \rightarrow 0} [s\phi_t(s)] = 0$, the arguments from Results II-III imply that in Regime II the extra contribution to the score due to ϕ_t vanishes, thus leading to a correct target distribution in high-dimensions. The freedom in the choice of ϕ_t can be used to improve the effect of CFG in Regime I, helping to push the system in the direction of class c , while reducing the unwanted finite-dimensional drawbacks. In the following, as a proof of principle, we propose a first example for ϕ_t (another is discussed in App. G). As we shall show, this choice already allows to improve state-of-the-art generative models. Ultimately, the whole function ϕ_t may be optimized as a hyperparameter.

5.2 Power-law CFG

We choose $\phi_t(s) = \omega s^\alpha$ with $\alpha > -1$ to obtain the following guidance scheme:

$$\vec{S}_t^{\text{PL}}(\vec{x}, c) = S_t(\vec{x}, c) + \omega [S_t(\vec{x}, c) - S_t(\vec{x})] \left| \vec{S}_t(\vec{x}, c) - \vec{S}_t(\vec{x}) \right|^\alpha. \quad (8)$$

One can understand the effect of non-linear guidance as follows. The ℓ_2 distance between scores $\delta S_t = |\vec{S}_t(\vec{x}, c) - \vec{S}_t(\vec{x})|$ is exponentially small both at the beginning of the backward process (as both cond. and uncond. distributions are standard Gaussian) and before exiting Regime I (as shown in Section 4), after which it remains zero. The non-linear scheme, while automatically switching off in Regime II, allows altering the shape of δS_t during Regime I. Choosing $\alpha < 0$ provides guidance which speeds up convergence to the target at early times, while $\alpha > 0$ dampens the guidance for small δS_t and strengthens it for large δS_t . In practice, we found positive values for α to perform best.

Additional Non-Linear CFG forms. We note that the framework in Eq. (7) covers many concurrent works on alternative CFG forms: with $\phi_t(s) = \omega \cdot \mathbb{I}_{[t_1, t_2]}(t)$, we obtain limited-interval CFG by Kynkäänniemi et al. (2024). Using $\phi_t(s) = \omega_t$ yields CFG weight schedulers as in Wang et al. (2024); Gao et al. (2023). Guidance schemes by Chung et al. (2024); Xia et al. (2024); Ventura et al. (2024) also yield simple $\phi_t(s)$ expressions. However, all of the aforementioned works use a guidance term that is linear in the score difference δS_t . In the experiments below, we find that non-linear power-law guidance \vec{S}_t^{PL} improves over these existing linear methods.

5.3 Generative image model experiments

Experimental details. We examine power-law CFG (8) GMM simulations, and four generative models: DiT (Peebles and Xie, 2023) and EDM2 (Karras et al., 2024b), trained and evaluated on ImageNet-1K (resolutions 256 and 512). We also consider two text-to-image models: first is trained on ImageNet-1K and CC12M (Changpinyo et al., 2021), evaluated on CC12M, using the diffusion DDPM training objective (Ho et al., 2020) with MMDiT architecture (Esser et al. (2024), similar to SD3). The second model, using MMDiT scaled to 1.6B parameters, is trained with flow matching on YFCC100M (Thomee et al., 2016), CC12M and a proprietary dataset of 320M Shutterstock images, evaluated on COCO dataset (Lin et al., 2014). App. F contains a third text-to-image model trained with DDPM objective with the MDTv2 (Gao et al., 2023) architecture scaled to 800M parameters.

We blurred human faces in ImageNet-1K and CC12M, and utilized Florence-2 (Xiao et al., 2023) to recaption images for more accurate image content descriptions.

Comparing GMM simulations to real-world experiments. In Figure 4 (first and third panel) we observe similar hump-shaped behavior of the difference between conditional and unconditional score $|S_t(\vec{x}, c) - S_t(\vec{x})|$ for GMMs and real-world models, validating the applicability of our theoretical findings. Furthermore, using the parameter α in Power-law CFG, we can alter the shape of these curves, obtaining a more flexible framework

Table 1 Power-law CFG often improves both fidelity and diversity metrics. We applied power-law to standard CFG and limited and CADs variants, as the two were the strongest competitors. Applying power-law improved their performance further, achieving competitive results. Best results are **bolded**, second best underlined. (\uparrow) indicates power-law CFG improves the guidance method compared to its version with stand. CFG, while (\downarrow) means the metric deteriorated. T2IM represents text-to-image models, CC class-conditional; FM is short for flow-matching objective and diff. stands diffusion. Experimental details are provided in App. F.

Model	EDM2-S (CC, IM-1K 512)			DiT/XL-2 (CC, IM-1K 256)			Diff. MMDiT (T2IM, CC12m)			FM MMDiT (T2IM, COCO)		
	FID	Precision	Recall	FID	Precision	Recall	FID	Precision	Recall	FID	Precision	Recall
Standard (Ho and Salimans, 2022)	2.29	0.751	0.582	2.27	0.829	0.584	8.58	0.661	0.569	5.20	0.629	0.594
Scheduler (Wang et al., 2024)	2.03	0.762	0.591	2.14	0.840	0.614	8.30	0.681	0.559	5.00	0.606	0.623
Limited (Kynkäänniemi et al., 2024)	1.87	0.760	0.598	1.97	0.801	0.632	8.58	0.680	0.553	5.00	0.609	0.602
Cosine (Gao et al., 2023)	2.15	0.770	0.619	2.30	0.861	0.520	8.29	0.659	0.564	5.14	0.630	0.616
CADS (Sadat et al., 2023)	<u>1.60</u>	0.792	0.619	<u>1.70</u>	0.772	0.627	8.32	0.692	0.559	4.91	<u>0.633</u>	0.613
APG (Sadat et al., 2024)	2.13	0.756	0.640	2.11	0.815	0.628	8.49	0.661	<u>0.571</u>	5.23	0.614	0.631
REG (Xia et al., 2024)	1.99	0.761	0.608	1.76	0.799	0.601	<u>8.10</u>	0.673	0.540	5.06	0.619	0.619
CFG++ (Chung et al., 2024)	N/A	N/A	N/A	N/A	N/A	N/A	8.35	0.668	0.552	4.85	0.632	0.629
Power-law CFG (Ours)	1.93 (\downarrow)	<u>0.780</u> (\uparrow)	<u>0.631</u> (\uparrow)	2.05 (\downarrow)	0.831 (\uparrow)	0.595 (\uparrow)	8.11 (\downarrow)	0.670 (\uparrow)	0.553 (\downarrow)	<u>4.81</u> (\downarrow)	0.621 (\downarrow)	0.619 (\uparrow)
Power-law CFG + Limited (Ours)	1.73 (\downarrow)	0.752 (\downarrow)	0.600 (\uparrow)	1.87 (\downarrow)	<u>0.849</u> (\uparrow)	0.642 (\uparrow)	8.27 (\downarrow)	0.692 (\uparrow)	0.555 (\uparrow)	4.84 (\downarrow)	0.615 (\uparrow)	0.622 (\uparrow)
Power-law CFG + CADs (Ours)	1.52 (\downarrow)	0.770 (\downarrow)	0.622 (\uparrow)	1.63 (\downarrow)	0.754 (\downarrow)	<u>0.639</u> (\uparrow)	7.98 (\downarrow)	<u>0.690</u> (\downarrow)	0.573 (\uparrow)	4.71 (\downarrow)	0.640 (\uparrow)	<u>0.624</u> (\downarrow)

generalizing standard CFG (see Figure 4 central panel). This enables faster convergence, and as we show in Figure 28 in App. G yielding paths with consistently smaller Jensen-Shannon divergence to the target distribution across all time τ and reducing the overshoot of the target distribution.

Power-law CFG is robust. We perform sensitivity analysis, showing that large values of α consistently yield improved performance, increasing robustness and stability when tuning for ω .³ This is shown in Figure 5 for EDM2-S and in App. F for DiT/XL-2 and two T2IM models, together with further ablation studies showing that non-linear CFG consistently outperforms standard CFG when varying number of sampling steps.

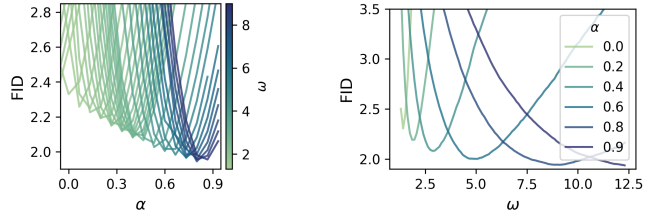


Figure 5 Sensitivity analysis (EDM2-S, ImageNet-1K 512 \times 512). **Left:** Increasing parameter α consistently improves FID to standard CFG ($\alpha = 0.0$). **Right:** Increasing α yields more stable FID values across a larger range of ω .

Power-law CFG improves image quality and diversity. We quantitatively evaluate our method using FID (Heusel et al., 2017) measuring image quality, and precision and recall (Sajjadi et al., 2018) measuring diversity. In Table 1, we compare power-law CFG to standard CFG and recent state-of-the-art guidance methods. As power-law guidance is easily combined with other guidance approaches, we also include results where we combine it with CADs (Sadat et al., 2023) and limited-guidance (Kynkäänniemi et al., 2024), which we found to be the strongest competitors. Power-law CFG improves over standard CFG in most cases (see arrows in table), and similarly it improves results of CADs and limited-interval guidance. Moreover, the latter combinations lead to results improving over existing approaches in many cases. We provide qualitative results in Figure 6, observing that power-law CFG improves both quality and diversity, while again being more robust to changing ω .

We provide additional qualitative examples in F for class-conditional and text-to-image models, as well as extend the quantitative results using additional metrics.

6 Conclusion

We studied the theoretical foundations of CFG, extending previous results to high and infinite-dimensional settings. Our research revealed that in sufficiently high dimension, CFG is in fact able to reproduce the correct target distribution, yielding a "blessing-of-dimensionality" result. Building on our theoretical analysis, we placed CFG in a larger family of guidance strategies, proposing a simple non-linear CFG extension.

³Although power-law CFG introduces another hyperparameter, α , we did not have to perform extensive hyperparameter search, and found large values, *e.g.*, $\alpha = 0.9$ to consistently perform well.

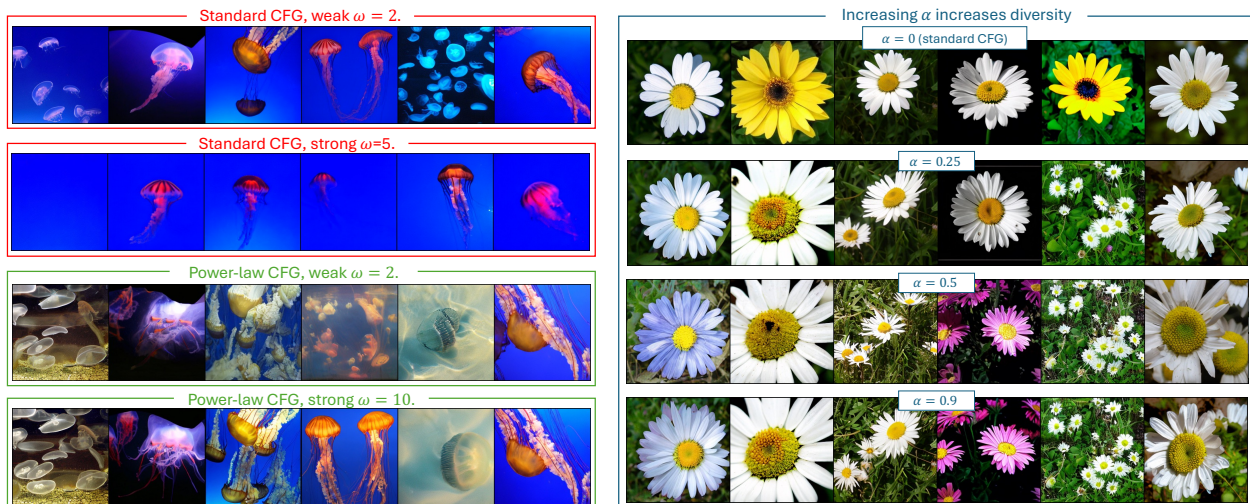


Figure 6 Qualitative comparison of Standard and Power-Law CFG on DiT/XL-2 trained on ImageNet-1K (256×256). **Left:** while standard CFG results in diversity decrease or mode collapse (first image for $\omega = 5$), power-law CFG ($\alpha = 0.9$) improves in diversity at no cost to fidelity, showing robustness to varying of ω (note very large $\omega = 10$). **Right:** Increasing non-linear parameter α yields larger diversity, while preserving image quality. Experimental details with further examples (as well as text-to-image) are provided in App. F.

We confirmed its effectiveness through numerical and real-world experiments, applying it successfully to state-of-the-art text-to-image and class-conditional models. Our results demonstrate its consistent ability to improve sample quality and diversity.

Limitations and future work. Our theory demonstrates that in high-dimensional settings, CFG generates the correct target distribution, extending previous results showing CFG alters it in low-dimensions. In practice, CFG improves fidelity while reducing diversity: although our theory allows discovery of guidances that maintain strong fidelity while significantly boosting diversity, the reason why CFG-modified distribution is more effective in practice is not explained by our theory which relies on perfect score estimation. We hypothesize, therefore, that the practical benefits of (non-linear) CFG might be tied to the imperfect score estimators used in practice. Investigating how score approximation errors impact guidance effectiveness is an important area for future research. Another key area of future study includes designing new non-linear CFG approaches.

Acknowledgements

This work has received funding from the French government, managed by the National Research Agency (ANR), under the France 2030 program with the reference ANR-23-IACL-0008. Furthermore, this paper is supported by PNRR-PE-AI FAIR project funded by the NextGeneration EU program. We would like to thank Mathurin Videau, João Maria Janeiro, Kunhao Zheng, Tariq Berrada Ifriqi, Wes Bouaziz and Tony Bonnaire for fruitful discussions regarding the numerical experiments. We would further like to thank Levent Sagun, David Lopez-Paz, Brian Karrer, Ricky Chen, Arnaud Doucet, Yaron Lipman and Luke Zettlemoyer for feedback and support. Finally, we also thank Carolyn Krol and Carolina Braga for extensive consultation and support throughout this project.

References

- Beatrice Achilli, Luca Ambrogioni, Carlo Lucibello, Marc Mézard, and Enrico Ventura. Memorization and generalization in generative diffusion under the manifold hypothesis. *arXiv preprint arXiv:2502.09578*, 2025.
- Michael S Albergo, Nicholas M Boffi, and Eric Vanden-Eijnden. Stochastic interpolants: A unifying framework for flows and diffusions. *arXiv preprint arXiv:2303.08797*, 2023.
- Santiago Aranguri, Giulio Biroli, Marc Mezard, and Eric Vanden-Eijnden. Optimizing noise schedules of generative models in high dimensions. *arXiv preprint arXiv:2501.00988*, 2025.
- Pietro Astolfi, Marlene Careil, Melissa Hall, Oscar Mañas, Matthew Muckley, Jakob Verbeek, Adriana Romero Soriano, and Michal Drozdal. Consistency-diversity-realism Pareto fronts of conditional image generative models. *arXiv preprint*, 2406.10429, 2024.
- Stefano Bae, Enzo Marinari, and Federico Ricci-Tersenghi. A very effective and simple diffusion reconstruction for the diluted ising model. *arXiv preprint arXiv:2407.07266*, 2024.
- Weimin Bai, Yifei Wang, Wenzheng Chen, and He Sun. An expectation-maximization algorithm for training clean diffusion models from corrupted observations. *arXiv preprint arXiv:2407.01014*, 2024.
- James Betker, Gabriel Goh, Li Jing, Tim Brooks, Jianfeng Wang, Linjie Li, Long Ouyang, Juntang Zhuang, Joyce Lee, Yufei Guo, et al. Improving image generation with better captions. *Computer Science*. <https://cdn.openai.com/papers/dall-e-3.pdf>, 2(3):8, 2023.
- Giulio Biroli and Marc Mézard. Generative diffusion in very large dimensions. *Journal of Statistical Mechanics: Theory and Experiment*, 2023(9):093402, 2023.
- Giulio Biroli, Tony Bonnaire, Valentin De Bortoli, and Marc Mézard. Dynamical regimes of diffusion models. *arXiv preprint arXiv:2402.18491*, 2024.
- Arwen Bradley and Preetum Nakkiran. Classifier-free guidance is a predictor-corrector. *arXiv preprint arXiv:2408.09000*, 2024.
- Soravit Changpinyo, Piyush Sharma, Nan Ding, and Radu Soricut. Conceptual 12m: Pushing web-scale image-text pre-training to recognize long-tail visual concepts. In *Proceedings of the IEEE/CVF conference on computer vision and pattern recognition*, pages 3558–3568, 2021.
- Muthu Chidambaram, Khashayar Gatmiry, Sitan Chen, Holden Lee, and Jianfeng Lu. What does guidance do? a fine-grained analysis in a simple setting. *arXiv preprint*, 2409.13074, 2024.
- Hyungjin Chung, Jeongsol Kim, Geon Yeong Park, Hyelin Nam, and Jong Chul Ye. Cfg++: Manifold-constrained classifier free guidance for diffusion models. *arXiv preprint arXiv:2406.08070*, 2024.
- Hugo Cui, Florent Krzakala, Eric Vanden-Eijnden, and Lenka Zdeborová. Analysis of learning a flow-based generative model from limited sample complexity. *arXiv preprint arXiv:2310.03575*, 2023.
- Jia Deng, Wei Dong, Richard Socher, Li-Jia Li, Kai Li, and Li Fei-Fei. Imagenet: A large-scale hierarchical image database. In *2009 IEEE conference on computer vision and pattern recognition*, pages 248–255. Ieee, 2009.
- Prafulla Dhariwal and Alexander Nichol. Diffusion models beat gans on image synthesis. In *Advances in neural information processing systems*, 2021.
- Yilun Du, Conor Durkan, Robin Strudel, Joshua B Tenenbaum, Sander Dieleman, Rob Fergus, Jascha Sohl-Dickstein, Arnaud Doucet, and Will Sussman Grathwohl. Reduce, reuse, recycle: Compositional generation with energy-based diffusion models and mcmc. In *International conference on machine learning*, pages 8489–8510. PMLR, 2023.
- Patrick Esser, Sumith Kulal, Andreas Blattmann, Rahim Entezari, Jonas Müller, Harry Saini, Yam Levi, Dominik Lorenz, Axel Sauer, Frederic Boesel, et al. Scaling rectified flow transformers for high-resolution image synthesis. In *Forty-first International Conference on Machine Learning*, 2024.
- Shanghua Gao, Pan Zhou, Ming-Ming Cheng, and Shuicheng Yan. Masked diffusion transformer is a strong image synthesizer. In *Proceedings of the IEEE/CVF International Conference on Computer Vision*, pages 23164–23173, 2023.
- Anand Jerry George, Rodrigo Veiga, and Nicolas Macris. Analysis of diffusion models for manifold data. *arXiv preprint arXiv:2502.04339*, 2025.

- Melissa Hall, Oscar Mañas, Reyhane Askari, Mark Ibrahim, Candace Ross, Pietro Astolfi, Tariq Berrada Ifriqi, Marton Havasi, Yohann Benchetrit, Karen Ullrich, et al. Evalgin: A library for evaluating generative image models. *arXiv preprint arXiv:2412.10604*, 2024.
- Martin Heusel, Hubert Ramsauer, Thomas Unterthiner, Bernhard Nessler, and Sepp Hochreiter. Gans trained by a two time-scale update rule converge to a local nash equilibrium. *Advances in neural information processing systems*, 30, 2017.
- Jonathan Ho and Tim Salimans. Classifier-free diffusion guidance. *arXiv preprint arXiv:2207.12598*, 2022.
- Jonathan Ho, Ajay Jain, and Pieter Abbeel. Denoising diffusion probabilistic models, 2020. <https://arxiv.org/abs/2006.11239>.
- Zahra Kadkhodaie, Stéphane Mallat, and Eero P Simoncelli. Feature-guided score diffusion for sampling conditional densities. *arXiv preprint arXiv:2410.11646*, 2024.
- Tero Karras, Miika Aittala, Timo Aila, and Samuli Laine. Elucidating the design space of diffusion-based generative models. *Advances in neural information processing systems*, 35:26565–26577, 2022.
- Tero Karras, Miika Aittala, Tuomas Kynkäänniemi, Jaakko Lehtinen, Timo Aila, and Samuli Laine. Guiding a diffusion model with a bad version of itself. *arXiv preprint arXiv:2406.02507*, 2024a.
- Tero Karras, Miika Aittala, Jaakko Lehtinen, Janne Hellsten, Timo Aila, and Samuli Laine. Analyzing and improving the training dynamics of diffusion models. In *Proceedings of the IEEE/CVF Conference on Computer Vision and Pattern Recognition*, pages 24174–24184, 2024b.
- Tuomas Kynkäänniemi, Miika Aittala, Tero Karras, Samuli Laine, Timo Aila, and Jaakko Lehtinen. Applying guidance in a limited interval improves sample and distribution quality in diffusion models. *arXiv preprint arXiv:2404.07724*, 2024.
- Marvin Li and Sitan Chen. Critical windows: non-asymptotic theory for feature emergence in diffusion models. *arXiv preprint arXiv:2403.01633*, 2024.
- Yingyu Liang, Zhenmei Shi, Zhao Song, and Yufa Zhou. Unraveling the smoothness properties of diffusion models: A gaussian mixture perspective. *arXiv preprint arXiv:2405.16418*, 2024.
- Tsung-Yi Lin, Michael Maire, Serge Belongie, James Hays, Pietro Perona, Deva Ramanan, Piotr Dollár, and C Lawrence Zitnick. Microsoft coco: Common objects in context. In *Computer Vision—ECCV 2014: 13th European Conference, Zurich, Switzerland, September 6–12, 2014, Proceedings, Part V 13*, pages 740–755. Springer, 2014.
- Yaron Lipman, Ricky TQ Chen, Heli Ben-Hamu, Maximilian Nickel, and Matt Le. Flow matching for generative modeling. *arXiv preprint arXiv:2210.02747*, 2022.
- Yaron Lipman, Marton Havasi, Peter Holderrieth, Neta Shaul, Matt Le, Brian Karrer, Ricky TQ Chen, David Lopez-Paz, Heli Ben-Hamu, and Itai Gat. Flow matching guide and code. *arXiv preprint arXiv:2412.06264*, 2024.
- Xingchao Liu, Chengyue Gong, and Qiang Liu. Flow straight and fast: Learning to generate and transfer data with rectified flow. *arXiv preprint arXiv:2209.03003*, 2022.
- Alex Nichol, Prafulla Dhariwal, Aditya Ramesh, Pranav Shyam, Pamela Mishkin, Bob McGrew, Ilya Sutskever, and Mark Chen. Glide: Towards photorealistic image generation and editing with text-guided diffusion models. *arXiv preprint arXiv:2112.10741*, 2021.
- William Peebles and Saining Xie. Scalable diffusion models with transformers. In *Proceedings of the IEEE/CVF International Conference on Computer Vision*, pages 4195–4205, 2023.
- Gabriel Raya and Luca Ambrogioni. Spontaneous symmetry breaking in generative diffusion models. *Advances in Neural Information Processing Systems*, 36, 2024.
- Seyedmorteza Sadat, Jakob Buhmann, Derek Bradley, Otmar Hilliges, and Romann M Weber. Cads: Unleashing the diversity of diffusion models through condition-annealed sampling. *arXiv preprint arXiv:2310.17347*, 2023.
- Seyedmorteza Sadat, Otmar Hilliges, and Romann M Weber. Eliminating oversaturation and artifacts of high guidance scales in diffusion models. In *The Thirteenth International Conference on Learning Representations*, 2024.
- Chitwan Saharia, William Chan, Saurabh Saxena, Lala Li, Jay Whang, Emily L Denton, Kamyar Ghasemipour, Raphael Gontijo Lopes, Burcu Karagol Ayan, Tim Salimans, et al. Photorealistic text-to-image diffusion models with deep language understanding. *Advances in neural information processing systems*, 35:36479–36494, 2022.

- Mehdi SM Sajjadi, Olivier Bachem, Mario Lucic, Olivier Bousquet, and Sylvain Gelly. Assessing generative models via precision and recall. *Advances in neural information processing systems*, 31, 2018.
- Tim Salimans, Ian Goodfellow, Wojciech Zaremba, Vicki Cheung, Alec Radford, and Xi Chen. Improved techniques for training gans. *Advances in neural information processing systems*, 29, 2016.
- Antonio Sclocchi, Alessandro Favero, and Matthieu Wyart. A phase transition in diffusion models reveals the hierarchical nature of data. *arXiv preprint arXiv:2402.16991*, 2024.
- Vikash Sehwal, Caner Hazirbas, Albert Gordo, Firat Ozgenel, and Cristian Canton. Generating high fidelity data from low-density regions using diffusion models. In *Proceedings of the IEEE/CVF Conference on Computer Vision and Pattern Recognition*, pages 11492–11501, 2022.
- Kulin Shah, Sitan Chen, and Adam Klivans. Learning mixtures of gaussians using the ddpm objective. *Advances in Neural Information Processing Systems*, 36:19636–19649, 2023.
- Jascha Sohl-Dickstein, Eric A. Weiss, Niru Maheswaranathan, and Surya Ganguli. Deep unsupervised learning using nonequilibrium thermodynamics, 2015. <https://arxiv.org/abs/1503.03585>.
- Yang Song and Stefano Ermon. Generative modeling by estimating gradients of the data distribution, 2020. <https://arxiv.org/abs/1907.05600>.
- Yang Song, Jascha Sohl-Dickstein, Diederik P Kingma, Abhishek Kumar, Stefano Ermon, and Ben Poole. Score-based generative modeling through stochastic differential equations. *arXiv preprint arXiv:2011.13456*, 2020a.
- Shikun Sun, Longhui Wei, Zhicai Wang, Zixuan Wang, Junliang Xing, Jia Jia, and Qi Tian. Inner classifier-free guidance and its taylor expansion for diffusion models. In *The Twelfth International Conference on Learning Representations*, 2023.
- Bart Thomee, David A Shamma, Gerald Friedland, Benjamin Elizalde, Karl Ni, Douglas Poland, Damian Borth, and Li-Jia Li. Yfcc100m: The new data in multimedia research. *Communications of the ACM*, 59(2):64–73, 2016.
- Enrico Ventura, Beatrice Achilli, Gianluigi Silvestri, Carlo Lucibello, and Luca Ambrogioni. Manifolds, random matrices and spectral gaps: The geometric phases of generative diffusion. *arXiv preprint arXiv:2410.05898*, 2024.
- Qing Wang, Sanjeev R Kulkarni, and Sergio Verdú. Divergence estimation for multidimensional densities via k -nearest-neighbor distances. *IEEE Transactions on Information Theory*, 55(5):2392–2405, 2009.
- Xi Wang, Nicolas Dufour, Nefeli Andreou, Marie-Paule Cani, Victoria Fernández Abrevaya, David Picard, and Vicky Kalogeiton. Analysis of classifier-free guidance weight schedulers. *arXiv preprint*, 2404.13040, 2024.
- Yuchen Wu, Minshuo Chen, Zihao Li, Mengdi Wang, and Yuting Wei. Theoretical insights for diffusion guidance: A case study for gaussian mixture models. *arXiv preprint arXiv:2403.01639*, 2024.
- Mengfei Xia, Nan Xue, Yujun Shen, Ran Yi, Tieliang Gong, and Yong-Jin Liu. Rectified diffusion guidance for conditional generation. *arXiv preprint arXiv:2410.18737*, 2024.
- Bin Xiao, Haiping Wu, Weijian Xu, Xiyang Dai, Houdong Hu, Yumao Lu, Michael Zeng, Ce Liu, and Lu Yuan. Florence-2: Advancing a unified representation for a variety of vision tasks (2023). URL <https://arxiv.org/abs/2311.06242>, 2023.
- Zhendong Yu and Haiping Huang. Nonequilibrium physics of generative diffusion models. *arXiv preprint arXiv:2405.11932*, 2024.
- Candi Zheng and Yuan Lan. Characteristic guidance: Non-linear correction for DDPM at large guidance scale. *arXiv preprint arXiv:2312.07586*, 2023.
- Jean Zinn-Justin. *Quantum field theory and critical phenomena*, volume 171. Oxford university press, 2021.

Appendix

The supplementary material is structured as follows:

- In Section A, we give a brief introduction to related work, focusing on [Biroli et al. \(2024\)](#).
- In Section B, we give proofs for two equidistant, symmetric Gaussian mixtures.
- In Section C, we present arguments how to extend the proofs to non-centered Gaussian mixtures (subsec. C.1) and multiple Gaussian mixtures (subsec. C.2).
- In Section D, we present the theoretical and numerical findings for finite dimension (including low dimension d).
- In Section E, we present experimental details for Gaussian mixture numerical simulations.
- In Section F, we provide experimental details involving real-world experiments.
- In Section G, we propose another non-linear CFG alternative and provide num. experiments.
- In Section H, we discuss the broader societal impact of our work.

A Introduction to related work: Classifier-free Guidance (CFG) and Specification Time in the High-Dimensional Limit

We start by briefly introducing the calculation required for estimating the speciation time t_s for a case of two equally weighted Gaussians. This section is a direct adaptation of the framework introduced by [Biroli et al. \(2024\)](#). The diffusion process, consisting of d independent Ornstein-Uhlenbeck Langevin equations, reads as follows (using $f(t) = -1$ and $g(t) = \sqrt{2}$ in [Eq. \(1\)](#)):

$$d\vec{x}(t) = -\vec{x}dt + d\vec{B}(t), \quad (9)$$

where $d\vec{B}(t)$ equals the square root of two times the standard Brownian motion in \mathbb{R}^d . At time $t = 0$, the process starts from the probability distribution $P_0(\vec{a})$, consisting of two Gaussian clusters that have means at $\pm\vec{m}$ and share the same variance σ^2 . To guarantee that these Gaussians remain distinct in high-dimensional space, we assume that $|\vec{m}|^2 = d\tilde{\mu}^2$, where both σ and $\tilde{\mu}$ are of order 1.

As the process evolves, the emergence of speciation resembles symmetry breaking observed during thermodynamic phase transitions. A common approach to analyzing this phenomenon is to construct a perturbative expansion of the free energy as a function of the field. Therefore, [Biroli et al. \(2024\)](#) derive an expression for $\log P_t(\vec{x})$ using a perturbative expansion in terms of e^{-t} , which is valid for large time values. This method is justified since speciation occurs at large times.

One can rewrite the probability to be at \vec{x} at time t as

$$\begin{aligned} P_t(\vec{x}) &= \int d\vec{a} P_0(\vec{a}) \frac{1}{\sqrt{2\pi\Delta_t^d}} \exp\left(-\frac{1}{2} \frac{(\vec{x} - \vec{a}e^{-t})^2}{\Delta_t}\right) \\ &= \frac{1}{\sqrt{2\pi\Delta_t}} \exp\left(-\frac{1}{2} \frac{\vec{x}^2}{\Delta_t} + g(\vec{x})\right), \end{aligned}$$

where the function $g(\vec{x})$, defined as

$$g(\vec{x}) = \log \int d\vec{a} P_0(\vec{a}) \exp\left(-\frac{1}{2} \frac{\vec{a}^2 e^{-2t}}{\Delta_t}\right) \exp\left(\frac{e^{-t}\vec{x} \cdot \vec{a}}{\Delta_t}\right)$$

can be viewed through a field-theoretic (or equivalently, a probabilistic) approach, where it serves as a generative function for connected correlations among the variables \vec{a} ([Zinn-Justin, 2021](#)). By expanding this

function at large times, one can show:

$$g(\vec{x}) = \frac{e^{-t}}{\Delta_t} \sum_{i=1}^d x_i \langle a_i \rangle + \frac{1}{2} \frac{e^{-2t}}{\Delta_t^2} \sum_{i,j=1}^d x_i x_j \left[\langle a_i a_j \rangle - \langle a_i \rangle \langle a_j \rangle \right] + O\left((xe^{-t})^3\right),$$

where we utilize the brackets $\langle \cdot \rangle$ to denote the expectation value with respect to the effective distribution $P_0(\vec{a})e^{-\vec{a}^2 e^{-2t}/(2\Delta_t)}$. Therefore, the expansion can be used to show that at large times:

$$\log P_t(\vec{x}) = C + \frac{e^{-t}}{\Delta_t} \sum_{i=1}^d x_i \langle a_i \rangle - \frac{1}{2\Delta_t} \sum_{i,j=1}^d x_i M_{ij} x_j + O\left((xe^{-t})^3\right),$$

where C is an \vec{x} -independent term and

$$M_{ij} = \delta_{ij} - e^{-2t} \left[\langle a_i a_j \rangle - \langle a_i \rangle \langle a_j \rangle \right].$$

The curvature of $\log P_t(\vec{x})$ is closely linked to the spectral properties of the matrix M . In the large time regime, M approaches the identity matrix, and consequently, all its eigenvalues are positive. However, a qualitative shift in shape occurs at the maximum time t_s , where the largest eigenvalue of M transitions through zero. This marks the onset of the **speciation time**, distinguished by a change in curvature of the effective potential $-\log P_t(\vec{x})$. In this case, it can be easily computed: the matrix M is given by $M_{ij} = (1 - \sigma^2 e^{-2t}) \delta_{ij} - e^{-2t} m_i m_j$ and its largest eigenvalue is $(1 - \sigma^2 e^{-2t} - d\tilde{\mu}^2 e^{-2t})$. We get therefore in the large d limit $t_s = \frac{1}{2} \log(d\tilde{\mu}^2)$ which up to subleading corrections identifies the speciation timescale as

$$t_s = \frac{1}{2} \log(d).$$

B Theoretical proofs: two equidistant, symmetric Gaussian mixtures

Asymptotic stochastic process in Regime I and symmetry breaking

In the limit of large dimensions, a comprehensive analytical examination of the dynamics in Regime I, taking place on time-scales $t_s + O(1) = (1/2) \log d + O(1)$, can be provided, specifically at the beginning of the backward process. Assuming no collapse (for further details, refer to [Biroli et al. \(2024\)](#)), an investigation into diffusion dynamics shows that the empirical distribution $P_t^e(\vec{x})$ at time t can be approximated with high accuracy by $P_t(\vec{x})$. This approximation represents the convolution of the initial distribution P_0 , comprising a mixture of Gaussians centered at $\pm \vec{m}$, and a diffusion kernel proportional to $e^{-(\vec{x} - \vec{a}e^{-t})^2/2}$. Consequently, the explicit expression for this approximation is

$$P_0(\vec{x}) = \frac{1}{2 \left(\sqrt{2\pi\sigma^2}\right)^d} \left[e^{-(\vec{x} - \vec{m})^2/(2\sigma^2)} + e^{-(\vec{x} + \vec{m})^2/(2\sigma^2)} \right], \text{ and} \quad (10)$$

$$P_t(\vec{x}) = \frac{1}{2 \left(\sqrt{2\pi\Gamma_t}\right)^d} \left[e^{-(\vec{x} - \vec{m}e^{-t})^2/(2\Gamma_t)} + e^{-(\vec{x} + \vec{m}e^{-t})^2/(2\Gamma_t)} \right]$$

where $\Gamma_t = \sigma^2 e^{-2t} + \Delta_t$ goes to 1 at large times. The log of this probability is

$$\log P_t(\vec{x}) = -\frac{\vec{x}^2}{2\Gamma_t} + \log \cosh \left(\vec{x} \cdot \vec{m} \frac{e^{-t}}{\Gamma_t} \right),$$

and hence the score reads

$$S_t^i(\vec{x}) = -\frac{x^i}{\Gamma_t} + m_i \frac{e^{-t}}{\Gamma_t} \tanh\left(\frac{\vec{x} \cdot \vec{m} e^{-t}}{\Gamma_t}\right). \quad (11)$$

As there are two classes: $+\vec{m}$ and $-\vec{m}$, the score conditioned to one class equals the score associated to a given Gaussian. Therefore, for the two classes we have:

$$\begin{aligned} +\vec{m} : S_t^i(\vec{x}, +) &= \frac{-x^i + m_i e^{-t}}{\Gamma_t}, \text{ and} \\ -\vec{m} : S_t^i(\vec{x}, -) &= \frac{-x^i - m_i e^{-t}}{\Gamma_t}. \end{aligned} \quad (12)$$

B.1 Result I: What is the role of classifier-free guidance?

Let us first analyze the ‘‘transverse’’ directions $\vec{v} \perp \vec{m}$. For these directions, for all ω , the score is the same and equals $\vec{S}_t^{\text{CFG}}(\vec{x}, c) \cdot \vec{v} = -\frac{\vec{x} \cdot \vec{v}}{\Gamma_t}$. Let us project the backward Eq. (2) on a unit vector $\vec{v} \perp \vec{m}$. We write $p = \vec{x} \cdot \vec{v}$, and the backward equation now reads $dp = p(1 - 2/\Gamma_{t_f - \tau})d\tau + \sqrt{2}dB$ which is the backward equation for a single Gaussian variable. When $\tau \rightarrow t_f$ the projection $p = \vec{x} \cdot \vec{v}$ is thus distributed as $\mathcal{N}(0, \sigma^2)$, for all values of ω .

Therefore, as all the components except the one in the \vec{m} direction are not affected, we can consider only the component along \vec{m} :

$$\vec{S}_{t_{\text{CFG}}}(\vec{x}, c) \cdot \frac{\vec{m}}{|\vec{m}|} = -\frac{\vec{x} \cdot \vec{m} / |\vec{m}|}{\Gamma_t} + \omega \frac{|\vec{m}|^2 e^{-t}}{|\vec{m}| \Gamma_t} \cdot \left\{ c - \tanh\left(\frac{\vec{x} \cdot \vec{m} e^{-t}}{\Gamma_t}\right) \right\} + \frac{|\vec{m}| e^{-t} c}{\Gamma_t}.$$

By denoting $\frac{\vec{x} \cdot \vec{m}}{|\vec{m}|} = q(t)$, where $|\vec{m}| = \sqrt{d}$, we can obtain the backward equation:

$$dx^i = (x^i + 2S_{t_{\text{CFG}}}^i) d\tau + d\eta_i(\tau),$$

where $\tau = t_f - t$, i.e., the backward time. Therefore, we can obtain for Regime I and by projecting onto the $\frac{\vec{m}}{|\vec{m}|}$ direction, we have that:

$$dq = dx^i \cdot \frac{\vec{m}}{|\vec{m}|} = \left(q + 2 \left[-q + e^{-(t_f - t_s - \tau)} \left((1 + \omega) - \omega \tanh\left(q e^{-(t_f - t_s - \tau)} \right) \right) \right] \right) d\tau + d\eta(\tau),$$

as, in Regime I, we have that $\Gamma_t \approx 1$, and also $\sqrt{d} = e^{-t_s}$.

Again, from this point onward by $t(\tau)$ we denote the backward time for ease of notation. This is like having an effective potential:

$$dq = -\frac{\partial V^{\text{CFG}}(q, \tau)}{\partial q} d\tau + d\eta(\tau),$$

where

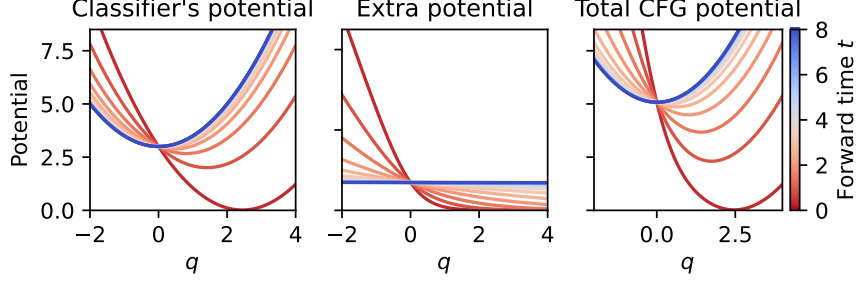


Figure 7 Effect of CFG on the guiding potential of a Gaussian mixture. The backward diffusion for the variable q giving the projection of \vec{x} on the center \vec{m} of the Gaussian where one wants to guide the backward diffusion. From left to right: Potential within the class, CFG-added-potential V_{extra} with $\omega = 2$, and their sum as in Eq. (6). CFG exhibits faster convergence to the target ($t = 0$), but results in narrower potential for small t (with t ranging from 0 to 8, as indicated on the right panel).

$$\begin{aligned}
 V^{\text{CFG}} &= \frac{1}{2}q^2 + 2 \left[-(1 + \omega)cqe^{-(t-t_s)} + \omega \ln \cosh \left(qe^{-(t-t_s)} \right) \right] \\
 &= \underbrace{\left(\frac{1}{2}q^2 - 2e^{-(t-t_s)}cq \right)}_{\text{Classifier's potential}} + \underbrace{\omega \left[-cqe^{-(t-t_s)} + \ln \cosh \left(qe^{-(t-t_s)} \right) \right]}_{\text{Extra potential } V_{\text{extra}}}.
 \end{aligned}$$

Therefore, for class $c = +1$ (equivalently for $c = -1$), there is little effect for $qe^{-(t-t_s)} \gg 1$, as then $-qe^{-(t-t_s)} + \ln \cosh \left(qe^{-(t-t_s)} \right) \approx 0$. Instead, for $qe^{-(t-t_s)} \ll -1$, we have that $-qe^{-(t-t_s)} + \ln \cosh \left(qe^{-(t-t_s)} \right) \approx -qe^{-(t-t_s)} \gg 1$. Therefore, we can conclude our first result:

Result I. In Regime I, before speciation time t_s , CFG is effective in aiding class selection and speeds up the convergence towards the target class c .

The utility of CFG is therefore to "push" in the right direction in Regime I where arguably the class-based score/potential is likely not accurate in the rare region ($q > 0$ for $c = -1$ and $q < 0$ for $c = +1$). The behavior of the two potentials is displayed in Figure 7.

B.2 Result II: Path alignment

The role of CFG in Regime I is to push the trajectories more in the direction of the selected class. We recall that the SDE verified by q when pushed towards class $c = +1$ reads:

$$dq = \left(q + 2 \left[-q + e^{-(t_f-t_s-\tau)} \left((1 + \omega) - \omega \tanh \left(qe^{-(t_f-t_s-\tau)} \right) \right) \right] \right) d\tau + d\eta(\tau), \quad (13)$$

For large times but still during Regime I, i.e. $t_f - t_s \ll \tau \ll \sqrt{d}$, q is very large (positive or negative). In this regime the CFG term can be neglected as it leads to exponentially small corrections to the SDE (of order $e^{-2qe^{-(t_f-t_s-\tau)}}$) with $t_f - t_s - \tau \gg 1$. In consequence, in Regime I at large times, the SDE just reads:

$$dq = -q + 2e^{-(t_f-t_s-\tau)} + d\eta(\tau),$$

The effect of CFG is to lead to different values of q when entering this late regime of Regime I. We call these values $q(\tau_i)$ and denote τ_i the fixed time at which the CFG contribution can be neglected. The value $q(\tau_i)$ is quickly (exponentially) forgotten when τ departs from τ_i , i.e., the evolution readjusts to the correct value without CFG. This can be shown by solving the SDE starting from a given τ_i :

$$q(\tau) = q(\tau_i)e^{-(\tau-\tau_i)} + e^{-(t_f-t_s)} \left(e^\tau - e^{-\tau+2\tau_i} \right) + \sqrt{1 - e^{-(2(\tau-\tau_i))}} z_\tau$$

where z_τ is a Gaussian variable with mean zero and unit variance. When $\tau \gg \tau_i$ but still in Regime I the solution of the SDE does not depend any longer on $q(\tau_i)$ and it coincides statistically with the one of the backward process of the single Gaussian corresponding to the class $c = +1$. This allows to conclude the second result:

Result II. Just before speciation time t_s , CFG-guided paths realign with the unguided path that generates the correct, unmodified target distribution.

B.3 Result III: When does classifier-free guidance take effect?

We can proceed to answer this question by examining the classifier-free guidance score, as defined in [Ho and Salimans \(2022\)](#):

$$S_{t_{CFG}}^i(\vec{x}, c) = (1 + \omega)S_t^i(\vec{x}, c) - \omega S_t^i(\vec{x}), \quad (14)$$

where $c = \pm 1$ and $\omega > 0$. By plugging in the cond. (12) and uncond. scores (11), we can obtain:

$$\begin{aligned} S_{t_{CFG}}^i(\vec{x}, c) &= -\frac{x^i}{\Gamma_t} + (1 + \omega)\frac{cm_i e^{-t}}{\Gamma_t} - \omega\frac{m_i e^{-t}}{\Gamma_t} \tanh\left(\frac{\vec{x} \cdot \vec{m} e^{-t}}{\Gamma_t}\right) \\ &= -\frac{x^i}{\Gamma_t} + \omega\frac{m_i e^{-t}}{\Gamma_t} \left\{ c - \tanh\left(\frac{\vec{x} \cdot \vec{m} e^{-t}}{\Gamma_t}\right) \right\} + \frac{cm_i e^{-t}}{\Gamma_t}. \end{aligned} \quad (15)$$

Now, in Regime II, when the trajectory has committed to a given class, $\vec{x} \cdot \vec{m} \sim O(d)$ and $\text{sign}(\vec{x} \cdot \vec{m}) = c$. Therefore, $c - \tanh\left(\frac{\vec{x} \cdot \vec{m} e^{-t}}{\Gamma_t}\right) \approx 0$, and one finds from (15), that $S_{t_{CFG}}^i(\vec{x}, c) = S_t^i(\vec{x})$. This implies that, within this regime, classifier-free guidance equals the conditional score. Therefore, Classifier free-guidance only affects Regime I, as $S_{t_{CFG}}^i(\vec{x}, c) = S_t^i(\vec{x})$ for $t > t_s = \frac{1}{2} \log(d)$. This allows us to conclude the third result:

Result III. In Regime II, after speciation time t_s , CFG has no effect on the generation process.

C Generalizations of the proof

In this section, we present arguments for extending our proofs to more general cases. We start by discussing proof generalization for non-centered Gaussian mixtures (Section C.1) and then move on to a mixture of four Gaussians (C.2). Finally, we conclude with some remarks on how to further extend these results to more complex scenarios.

C.1 Generalization to non-centered Gaussian mixtures

Asymptotic stochastic process in Regime I and symmetry breaking

Here we provide an example on how to generalize the study of Gaussian mixtures to the case where the two Gaussians are centered in \vec{m}_1 and \vec{m}_2 . We take \vec{m}_1, \vec{m}_2 as two arbitrary vectors in d dimensions, on the sphere $|\vec{m}_c|^2 = d$ the case where they have different norms, both scaling proportionally to d , could be studied as well with the same formalism.

The initial probability density is

$$P_0(\vec{x}) = \frac{1}{2 \left(\sqrt{2\pi\sigma^2}\right)^d} \left[e^{-(\vec{x}-\vec{m}_1)^2/(2\sigma^2)} + e^{-(\vec{x}-\vec{m}_2)^2/(2\sigma^2)} \right], \text{ and} \quad (16)$$

$$P_t(\vec{x}) = \frac{1}{2 \left(\sqrt{2\pi\Gamma_t} \right)^d} \left[e^{-(\vec{x}-\vec{m}_1 e^{-t})^2/(2\Gamma_t)} + e^{-(\vec{x}-\vec{m}_2 e^{-t})^2/(2\Gamma_t)} \right]$$

where $\Gamma_t = \sigma^2 e^{-2t} + \Delta_t$ goes to 1 at large times. The log of this probability is

$$\log P_t(\vec{x}) = -\frac{\vec{x}^2}{2\Gamma_t} + \log \left(e^{\vec{x} \cdot \vec{m}_1 \frac{e^{-t}}{\Gamma_t}} + e^{\vec{x} \cdot \vec{m}_2 \frac{e^{-t}}{\Gamma_t}} \right) + C,$$

where C is a constant, and hence the score reads

$$S_t^i(\vec{x}) = -\frac{x^i}{\Gamma_t} + \frac{e^{-t}}{\Gamma_t} \frac{m_1^i e^{\vec{x} \cdot \vec{m}_1 \frac{e^{-t}}{\Gamma_t}} + m_2^i e^{\vec{x} \cdot \vec{m}_2 \frac{e^{-t}}{\Gamma_t}}}{e^{\vec{x} \cdot \vec{m}_1 \frac{e^{-t}}{\Gamma_t}} + e^{\vec{x} \cdot \vec{m}_2 \frac{e^{-t}}{\Gamma_t}}} \quad (17)$$

As there are two classes: \vec{m}_1 and \vec{m}_2 , the score conditioned to one class equals the score associated to a given Gaussian. Therefore, for the two classes we have:

$$\begin{aligned} \vec{m}_1 : S_t^i(\vec{x}, +) &= \frac{-x^i + m_1^i e^{-t}}{\Gamma_t}, \text{ and} \\ \vec{m}_2 : S_t^i(\vec{x}, -) &= \frac{-x^i - m_2^i e^{-t}}{\Gamma_t}. \end{aligned} \quad (18)$$

What is the role of classifier-free guidance?

We shall use as basis the vectors $\vec{m}_+ = (\vec{m}_1 + \vec{m}_2)/2$, $\vec{m}_- = (\vec{m}_1 - \vec{m}_2)/2$, and we shall denote by \vec{v} the vectors orthogonal to the plane generated by \vec{m}_1, \vec{m}_2 .

For these ‘‘transverse’’ directions $\vec{v} \perp (\vec{m}_1, \vec{m}_2)$. for all ω , the score is the same and equals $\vec{S}_t^{\text{CFG}}(\vec{x}, c) \cdot \vec{v} = -\frac{\vec{x} \cdot \vec{v}}{\Gamma_t}$. Let us project the backward equation on a unit vector \vec{v} in the transverse space. We write $p = \vec{x} \cdot \vec{v}$, and the backward equation now reads $dp = p(1 - 2/\Gamma_{t_f - \tau})d\tau + \sqrt{2}dB$ which is the backward equation for a single Gaussian variable. When $\tau \rightarrow t_f$ the projection $p = \vec{x} \cdot \vec{v}$ is thus distributed as $\mathcal{N}(0, \sigma^2)$, for all values of ω .

Therefore, as all the components except the ones in the \vec{m}_+ and \vec{m}_- directions are not affected.

We now project the score on \vec{m}_+ and \vec{m}_- , using $\vec{m}_+ \cdot \vec{m}_- = 0$, $\vec{m}_+ \cdot \vec{m}_1 = \vec{m}_+ \cdot \vec{m}_2 = d^2/2$ and $\vec{m}_- \cdot \vec{m}_1 = -\vec{m}_- \cdot \vec{m}_2 = d^2/2$:

$$\begin{aligned} \vec{S}_{t_{\text{CFG}}}(\vec{x}, c) \cdot \vec{m}_+ &= \frac{(\vec{m}_+ e^{-t} - \vec{x}) \cdot \vec{m}_+}{\Gamma_t} \\ \vec{S}_{t_{\text{CFG}}}(\vec{x}, c) \cdot \vec{m}_- &= \frac{(\vec{m}_- e^{-t} - \vec{x}) \cdot \vec{m}_-}{\Gamma_t} + \omega \frac{|\vec{m}_-|^2 e^{-t}}{\Gamma_t} \cdot \left\{ 1 - \tanh \left(\frac{\vec{x} \cdot \vec{m}_- e^{-t}}{\Gamma_t} \right) \right\} \end{aligned}$$

Inserting these scores into the backward diffusion equation, one finds that:

- $\vec{x} \cdot \vec{m}_+ / |\vec{m}_+|$ evolves as a Gaussian variable. At time $\tau \rightarrow t_f$ the distribution of this variable is $\mathcal{N}(|\vec{m}_+|, \sigma^2)$.
- The variable $q_-(t) = \frac{\vec{x} \cdot \vec{m}_-}{|\vec{m}_-|}$ satisfies the same equation as the variable $q(t)$ which we analyzed in the ‘centered’ case where $\vec{m}_1 = -\vec{m}_2 = \vec{m}$

Therefore, we can conclude that in this case, CFG has the same effect: it is effective in aiding class selection, speeding up the convergence toward the correct target class c .

When does classifier-free guidance take effect?

We can proceed to answer this question by examining the classifier-free guidance score:

$$S_{t_{CFG}}^i(\vec{x}, c) = (1 + \omega)S_t^i(\vec{x}, c) - \omega S_t^i(\vec{x}), \quad (19)$$

where $c \in \{1, 2\}$ and $\omega > 0$. The CFG score guiding to class $c = 1$ is thus:

$$S_{t_{CFG}}^i(\vec{x}, c) = -\frac{x^i}{\Gamma_t} + (1 + \omega)\frac{m_1^i e^{-t}}{\Gamma_t} - \omega \frac{e^{-t} m_1^i e^{\vec{x} \cdot \vec{m}_1 \frac{e^{-t}}{\Gamma_t}} + m_2^i e^{\vec{x} \cdot \vec{m}_2 \frac{e^{-t}}{\Gamma_t}}}{e^{\vec{x} \cdot \vec{m}_1 \frac{e^{-t}}{\Gamma_t}} + e^{\vec{x} \cdot \vec{m}_2 \frac{e^{-t}}{\Gamma_t}}} \quad (20)$$

Now, in Regime II, when the trajectory has committed to a given class say class 1*, $\vec{x} \cdot \vec{m}_1 - \vec{x} \cdot \vec{m}_2$ is positive and of order $O(d)$. Therefore $S_{t_{CFG}}^i(\vec{x}, c) = S_t^i(\vec{x}, c)$. This implies that, within this regime, classifier-free guidance equals the conditional score. Therefore, Classifier free-guidance only affects Regime I, as $S_{t_{CFG}}^i(\vec{x}, c) = S_t^i(\vec{x})$ for $t > t_s = \frac{1}{2} \log(d)$. This allows us to conclude that in Regime II, CFG is innocuous.

Therefore all the results obtained for the centered case $\vec{m}_1 = -\vec{m}_2 = \vec{m}$ also hold for the more general case when the two Gaussians are centered in \vec{m}_1 and \vec{m}_2 .

C.2 Extension to the mixture of four Gaussians

Here we present the computation for a mixture of four Gaussians, in order to analyze the behavior of the system for an increasing number of classes and emphasize the extendability of our framework. As before, assuming no collapse, we can approximate the empirical distribution $P_t^e(\vec{x})$ at time t by $P_t(\vec{x})$ with high accuracy. In this case, the approximation represents the convolution of the initial distribution P_0 , being a mixture of 4 Gaussians centered at $\pm \vec{\mu}_1 \pm \vec{\mu}_2$, s.t. $\vec{\mu}_1 \cdot \vec{\mu}_2 = 0$, and a diffusion kernel proportional to $e^{-(\vec{x} - \vec{\mu} e^{-t})^2 / 2}$. The explicit expression for the distribution is:

$$P_0(\vec{x}) = \frac{1}{4 \left(\sqrt{2\pi\sigma^2} \right)^d} \left[e^{-(\vec{x} - (\vec{\mu}_1 - \vec{\mu}_2))^2 / (2\sigma^2)} + e^{-(\vec{x} - (\vec{\mu}_1 + \vec{\mu}_2))^2 / (2\sigma^2)} \right. \\ \left. + e^{-(\vec{x} + (\vec{\mu}_1 - \vec{\mu}_2))^2 / (2\sigma^2)} + e^{-(\vec{x} + (\vec{\mu}_1 + \vec{\mu}_2))^2 / (2\sigma^2)} \right]$$

and

$$P_t(\vec{x}) = \frac{1}{4 \left(\sqrt{2\pi\Gamma_t} \right)^d} \left[e^{-(\vec{x} - (\vec{\mu}_1 - \vec{\mu}_2)e^{-t})^2 / (2\Gamma_t)} + e^{-(\vec{x} - (\vec{\mu}_1 + \vec{\mu}_2)e^{-t})^2 / (2\Gamma_t)} \right. \\ \left. + e^{-(\vec{x} + (\vec{\mu}_1 - \vec{\mu}_2)e^{-t})^2 / (2\Gamma_t)} + e^{-(\vec{x} + (\vec{\mu}_1 + \vec{\mu}_2)e^{-t})^2 / (2\Gamma_t)} \right]$$

where $\Gamma_t = \sigma^2 e^{-2t} + \Delta_t$ goes to 1 at large times. This can be rewritten as:

$$P_t(\vec{x}) = \frac{1}{2 \left(\sqrt{2\pi\Gamma_t} \right)^d} e^{-(\vec{x}^2 + \vec{\mu}_1^2 e^{-2t} + \vec{\mu}_2^2 e^{-2t}) / (2\Gamma_t)} \left[e^{-\vec{\mu}_1 \cdot \vec{\mu}_2 e^{-2t} / \Gamma_t} \cosh \left(\vec{x} \cdot (\vec{\mu}_1 + \vec{\mu}_2) \frac{e^{-t}}{\Gamma_t} \right) \right. \\ \left. + e^{\vec{\mu}_1 \cdot \vec{\mu}_2 e^{-2t} / \Gamma_t} \cosh \left(\vec{x} \cdot (\vec{\mu}_1 - \vec{\mu}_2) \frac{e^{-t}}{\Gamma_t} \right) \right]$$

The log of this probability is:

$$\log P_t(\vec{x}) = \frac{-\vec{x}^2}{2\Gamma_t} + \log \left(e^{-\vec{\mu}_1 \cdot \vec{\mu}_2 e^{-2t}/\Gamma_t} \cosh \left(\vec{x} \cdot (\vec{\mu}_1 + \vec{\mu}_2) \frac{e^{-t}}{\Gamma_t} \right) + e^{\vec{\mu}_1 \cdot \vec{\mu}_2 e^{-2t}/\Gamma_t} \cosh \left(\vec{x} \cdot (\vec{\mu}_1 - \vec{\mu}_2) \frac{e^{-t}}{\Gamma_t} \right) \right)$$

And the score reads:

$$S_t^i(\vec{x}) = \frac{-x^i}{\Gamma_t} + \frac{e^{-t} (\vec{\mu}_1 + \vec{\mu}_2)_i e^{-\vec{\mu}_1 \cdot \vec{\mu}_2 e^{-2t}/\Gamma_t} \sinh \left(\vec{x} \cdot (\vec{\mu}_1 + \vec{\mu}_2) \frac{e^{-t}}{\Gamma_t} \right) + (\vec{\mu}_1 - \vec{\mu}_2)_i e^{\vec{\mu}_1 \cdot \vec{\mu}_2 e^{-2t}/\Gamma_t} \sinh \left(\vec{x} \cdot (\vec{\mu}_1 - \vec{\mu}_2) \frac{e^{-t}}{\Gamma_t} \right)}{e^{-\vec{\mu}_1 \cdot \vec{\mu}_2 e^{-2t}/\Gamma_t} \cosh \left(\vec{x} \cdot (\vec{\mu}_1 + \vec{\mu}_2) \frac{e^{-t}}{\Gamma_t} \right) + e^{\vec{\mu}_1 \cdot \vec{\mu}_2 e^{-2t}/\Gamma_t} \cosh \left(\vec{x} \cdot (\vec{\mu}_1 - \vec{\mu}_2) \frac{e^{-t}}{\Gamma_t} \right)}$$

As \vec{x} approaches one of the means $\pm \vec{\mu}_1 \pm \vec{\mu}_2$, the second summand reduces to $(\vec{\mu}_1 \pm \vec{\mu}_2) \tanh \left(\vec{x} \cdot (\vec{\mu}_1 \pm \vec{\mu}_2) \frac{e^{-t}}{\Gamma_t} \right)$ ⁴, resulting in an expression akin to the one for mixture of 2 Gaussians in (11).

Conclusion. The results above can be generalized to any finite number of Gaussians, centered around \vec{m}_i where \vec{m}_i is a vector of norm $\mu_i \sqrt{d}$. CFG will only have effect on space spanned by vectors \vec{m}_i and only in regime I. One can also consider non-isotropic Gaussians. As long as the covariance has eigenvalues not scaling with d , the backward process displays the two distinct regimes I and II, which is examined in detail for the mixture of two Gaussians. This result can be obtained by analyzing the forward process. The key point is that on all times of order one the noised Gaussian mixture still consists in non-overlapping Gaussian (regimeII). On times of order one close to the speciation time $1/2 \log d$ the Gaussians overlap and the center are of the same order of the noise (regime I). Because of the existence of these two regimes, the general arguments presented at the beginning of the paper hold and CFG does reproduce the correct distribution in the large d limit.

D Finite dimension

In this section, we give exact analyses describing the effect of CFG in finite- (possibly low-) dimensional settings, outlined in Section 4.3 in the main manuscript. We start the backward equation at a time t_f large enough that the distribution of x is a isotropic Gaussian with variance one. The backward equation for $x(t)$ with the CFG score reads:

$$\begin{aligned} \frac{dx_i}{d\tau} = & x_i \left(1 - \frac{2}{\Gamma(t_f - \tau)} \right) + \frac{2m_i}{\Gamma(t_f - \tau)} e^{-(t_f - \tau)} \\ & + 2\omega m_i \frac{e^{-(t_f - \tau)}}{\Gamma_{t_f - \tau}} \left\{ 1 - \tanh \left(\frac{\vec{x} \cdot \vec{m} e^{-(t_f - \tau)}}{\Gamma_{t_f - \tau}} \right) \right\} + \eta_i(\tau) \end{aligned} \quad (21)$$

where $\tau = 0$ at the beginning of the backward process and $\tau = t_f (\gg 1)$ at the end.

This can be projected on the evolution of the single parameter $q(\tau) = \vec{x} \cdot \vec{m} / \sqrt{d}$. We obtain

$$\begin{aligned} \frac{dq}{d\tau} = & q \left(1 - \frac{2}{\Gamma(t_f - \tau)} \right) + \frac{2\sqrt{d}}{\Gamma(t_f - \tau)} e^{-(t_f - \tau)} \\ & + 2\omega \sqrt{d} \frac{e^{-(t_f - \tau)}}{\Gamma_{t_f - \tau}} \left\{ 1 - \tanh \left(\frac{q\sqrt{d}e^{-(t_f - \tau)}}{\Gamma_{t_f - \tau}} \right) \right\} + \eta(\tau). \end{aligned} \quad (22)$$

⁴For large values of $x \cdot (\vec{\mu}_1 \pm \vec{\mu}_2) e^{-t}/\Gamma_t$, we utilized the *log-sum-exp trick* to calculate the value of the fraction.

Considering the right-hand side as a force due to a moving external potential $-\partial_q V(q, t)$, the effect of CFG is to add an extra term which has two main effects: (1) it adds a positive term to the force and, in consequence, it pushes q faster away from zero, (2) it increases the value of the Hessian at any point in q with respect to its $\omega = 0$ counterpart, thus making the potential more confining.

The initial condition is $q(\tau = 0) \sim \mathcal{N}(0, \sigma^2)$ and

$$\Gamma(t_f - \tau) = \sigma^2 e^{-2(t_f - \tau)} + 1 - e^{-2(t_f - \tau)}. \quad (23)$$

Case: $\omega = 0$

The solution of the backward equation is:

$$q(\tau) = q(0) e^{\tau - 2 \int_0^\tau \frac{1}{\Gamma(t_f - \tau'')} d\tau''} + \int_0^\tau \left[\frac{2\sqrt{d}e^{-(t_f - \tau')}}{\Gamma(t_f - \tau')} + \eta_i(\tau') \right] e^{(\tau - \tau') - 2 \int_{\tau'}^\tau \frac{1}{\Gamma(t_f - \tau'')} d\tau''} d\tau'. \quad (24)$$

Its probability distribution must coincide with the one of the solutions of the forward equation, which reads:

$$q(t) = \sqrt{d}e^{-t} + \sqrt{1 - e^{-2t}} z_i + e^{-t} \sigma \tilde{z}_i,$$

where $z_i, \tilde{z}_i \sim \mathcal{N}(0, 1)$ and $t = t_f - \tau$. Let us now focus on the mean of q . When we consider

$$\int_0^\tau \left[\frac{2\sqrt{d}e^{-(t_f - \tau')}}{\Gamma(t_f - \tau')} \right] e^{(\tau - \tau') - 2 \int_{\tau'}^\tau \frac{1}{\Gamma(t_f - \tau'')} d\tau''} d\tau',$$

using that

$$\frac{d}{d\tau'} \exp \left[-2 \int_{\tau'}^\tau \frac{1}{\Gamma(t_f - \tau'')} d\tau'' \right] = \frac{2}{\Gamma(t_f - \tau')} \exp \left[-2 \int_{\tau'}^\tau \frac{1}{\Gamma(t_f - \tau'')} d\tau'' \right],$$

one finds that the mean of q for the evolution with $\omega = 0$, starting from any value $q(0)$ at any time t_f , is

$$q(\tau) = q(0) e^{\tau - 2 \int_0^\tau \frac{1}{\Gamma(t_f - \tau'')} d\tau''} + \sqrt{d}e^{-(t_f - \tau)} \left(1 - \exp \left(-2 \int_0^\tau \frac{1}{\Gamma(t_f - \tau'')} d\tau'' \right) \right). \quad (25)$$

Using

$$\int_0^\tau \frac{1}{\Gamma(t_f - \tau'')} d\tau'' = -\frac{1}{2} \log \frac{e^{-2\tau} + (\sigma^2 - 1)e^{-2t_f}}{1 + (\sigma^2 - 1)e^{-2t_f}},$$

we find that

$$q(\tau) = q(0) e^\tau \frac{e^{-2\tau} + (\sigma^2 - 1)e^{-2t_f}}{1 + (\sigma^2 - 1)e^{-2t_f}} + \sqrt{d} e^{-(t_f - \tau)} \frac{1 - e^{-2\tau}}{1 + (\sigma^2 - 1)e^{-2t_f}}. \quad (26)$$

One can check that, when $q(0)$ is obtained by the equilibrium process with $\omega = 0$, namely $q(0) = \sqrt{d}e^{-t_f}$, then at all times $q(\tau) = \sqrt{d}e^{-(t_f - \tau)}$.

Case: interrupted guidance

Now let us consider a protocol of interrupted guidance. We start the backward process at $t_f \gg 1$ with a CFG coefficient $\omega > 0$. Then at time backward time τ_1 (forward time $t_1 = t_f - \tau_1$) we switch to $\omega = 0$. At time t_1 the mean of q obtained from the backward process with $\omega > 0$ is larger than the value $\sqrt{d}e^{-t_1}$ which would be obtained with the $\omega = 0$ dynamics (the reason is that the extra force in (22) is positive). Let us write this mean as

$$q(t_1, \omega) = \sqrt{d} e^{-t_1} + \delta q(t_1, \omega).$$

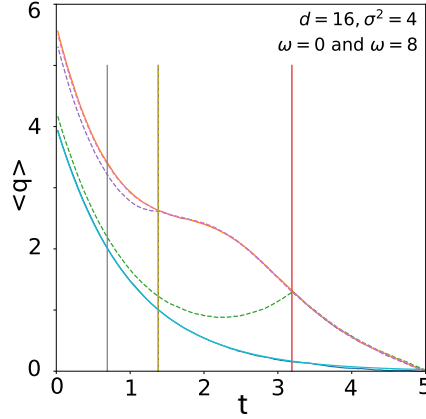


Figure 8 Mean value of q obtained from the backward diffusion in a Gaussian mixture model with $d = 16, \sigma^2 = 4$ (speciation time $t_s = 1.38$). The CFG is run with $\omega = 8$ from $t = 5$ to $t = t_1$, then one switches to the class guidance $\omega = 0$. The top curve is when CFG is kept all the time ($t_1 = 0$). The bottom curve is the case without CFG ($\omega = 0$). Three values of t_1 are studied $t_1 = 0.69, 1.38, 3.19$ (vertical lines). The dashed curves give the mean value of q for each of these three cases. They are in perfect agreement with the theoretical prediction (27).

Let us measure the backward time starting from $t = t_1$. We thus write $t = t_1 - \tilde{\tau}$. We can use formula (26) with $t_f \rightarrow t_1, \tau \rightarrow \tilde{\tau}$ and $q(0) \rightarrow q(t_1, \omega)$. This gives for the mean value of q :

$$\tilde{q}(\tilde{\tau}, \omega) = \sqrt{d}e^{-(t_1 - \tilde{\tau})} + \delta q(t_1, \omega) \frac{e^{-\tilde{\tau}} + (\sigma^2 - 1)e^{\tilde{\tau} - 2t_1}}{1 + (\sigma^2 - 1)e^{-2t_1}},$$

which, translated in terms of the forward time $t = t_1 - \tilde{\tau}$, gives:

$$q(t) = \sqrt{d}e^{-t} + \delta q(t_1, \omega) e^{t - t_1} \frac{1 + (\sigma^2 - 1)e^{-2t}}{1 + (\sigma^2 - 1)e^{-2t_1}}. \quad (27)$$

In particular at the end of the backward process, for $\tilde{\tau} = t_1$ we get

$$q(t = 0) = \sqrt{d} + \delta q(t_1, \omega) e^{-t_1} \frac{\sigma^2}{1 + (\sigma^2 - 1)e^{-2t_1}}$$

If we choose $t_1 = t_s = (1/2) \log d$, and assuming that the dynamics at $t > t_1$ has produced an average $q(t_1) = \sqrt{d}e^{-t_1} + \delta q$, we find that

$$q(t = 0) = \sqrt{d} \left(1 + \delta q \frac{\sigma^2/d}{1 + (\sigma^2 - 1)/d} \right).$$

This shows that the guidance interrupted at t_s gives a good result only in the limit $\sigma^2/d \ll 1$. Figs. 8 and 9 illustrate the effect of the choice of t_1 .

CFG contribution to the magnetization in Regime I

Using Equation (14), one can derive the equation for the average $\langle q(\tau) \rangle_\omega$:

$$\begin{aligned} \frac{d\langle q(\tau) \rangle_\omega}{d\tau} &= \langle q(\tau) \rangle_\omega \left(1 - \frac{2}{\Gamma(t_f - \tau)} \right) + \frac{2\sqrt{d}}{\Gamma(t_f - \tau)} e^{-(t_f - \tau)} \\ &+ 2\omega\sqrt{d} \frac{e^{-(t_f - \tau)}}{\Gamma(t_f - \tau)} \left\langle 1 - \tanh \left(\frac{q\sqrt{d}e^{-(t_f - \tau)}}{\Gamma(t_f - \tau)} \right) \right\rangle_\omega. \end{aligned} \quad (28)$$

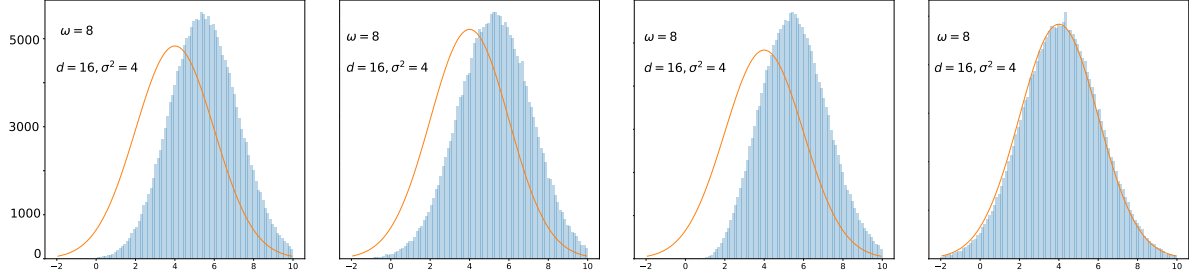


Figure 9 Histograms of $q(t=0)$ obtained from the backward diffusion in a Gaussian mixture model with $d = 16, \sigma^2 = 4$ (the speciation time is 1.38), run with 200,000 trajectories. Left: CFG with $\omega = 8$ is applied at all times. The final distribution has a larger mean and a smaller variance than the desired class distribution (full line). Next three figures: The CFG is run with $\omega = 8$ from $t = 5$ to $t = t_1$, then one switches to standard CFG $\omega = 0$. From left to right, $t_1 = 0.69, 1.38, 3.19$. The mean values of q in the four cases are respectively 5.56, 5.51, 5.29, 4.12 and the standard deviations 1.68, 1.74, 1.87, 1.98, with targets $\mu = 4, \sigma = 2$. In order to minimize the bias due to CFG one must interrupt it before the speciation takes place in the background diffusion, hence at $t_1 > t_s$.

The extra ω term is strictly positive. Therefore, we have:

$$\langle q(\tau) \rangle_\omega \geq \langle q(\tau) \rangle_{\omega=0}, \quad \forall \tau.$$

Moreover, using that the right-hand side is less than or equal to:

$$\langle q(\tau) \rangle_\omega \left(1 - \frac{2}{\Gamma(t_f - \tau)} \right) + \frac{2(1 + \omega)\sqrt{d}}{\Gamma(t_f - \tau)} e^{-(t_f - \tau)},$$

which corresponds to the backward equation one would obtain if $\|\vec{m}\|^2 = (1 + \omega)d$. We then find:

$$\langle q(\tau) \rangle_{\omega=0} < \langle q(\tau) \rangle_\omega < \sqrt{d} e^{-t} (1 + \omega).$$

We conclude that $\langle q(\tau) \rangle_\omega$ gets an extra contribution due to CFG of the order $\sqrt{d} e^{-t}$.

CFG indeed shifts the mean value. The amount of shift is of order $\sqrt{d} e^{-t}$ in Regime I. However, as we shall see next the CFG has almost no effect in Regime II, so we can use the result of the previous section to argue that the total shift due to CFG is the one of CFG in Regime I followed by a switch at $\omega = 0$ in Regime II, i.e., it is of order one.

CFG contribution to the score in Regime I vs in Regime II

Another interesting inequality can be derived for the difference between the CFG and the standard, non-guided score, $S_{\text{CFG}} - S_C$, evaluated on trajectories corresponding to CFG:

$$S_{\text{CFG}} - S_C = \omega \frac{\sqrt{d} e^{-(t_f - \tau)}}{\Gamma(t_f - \tau)} \left(1 - \tanh \left(\frac{q \sqrt{d} e^{-(t_f - \tau)}}{\Gamma(t_f - \tau)} \right) \right). \quad (29)$$

We use the fact that for the same thermal noise, we have $q_\omega(\tau) \geq q_{\omega=0}(\tau)$ because the CFG force is always equal or larger than the $\omega = 0$ one. Therefore for a given (the same) thermal history we have:

$$-\tanh \left(\frac{q_\omega(\tau) \sqrt{d} e^{-(t_f - \tau)}}{\Gamma(t_f - \tau)} \right) \leq -\tanh \left(\frac{q_{\omega=0}(\tau) \sqrt{d} e^{-(t_f - \tau)}}{\Gamma(t_f - \tau)} \right), \quad (30)$$

and we can obtain:

$$S_{\text{CFG}} - S_C \leq \frac{\sqrt{d}e^{-(t_f-\tau)}}{\Gamma(t_f-\tau)} \left(1 - \tanh \left(\frac{q_{\omega=0}(\tau)\sqrt{d}e^{-(t_f-\tau)}}{\Gamma(t_f-\tau)} \right) \right). \quad (31)$$

This inequality tells us, as expected, that the extra CFG contribution to the score is very small at the beginning of the backward process. Its mean increases, and is of the order of one during the backward process in Regime I. However, after the speciation time $q_{\omega=0}(\tau)$ is a Gaussian variable with a mean $\sqrt{d}e^{-(t_f-\tau)}$ much larger than the square root of the variance. Therefore, replacing the fluctuating variable by its mean we obtain

$$S_{\text{CFG}} - S_C \leq \frac{\sqrt{d}e^{-(t_f-\tau)}}{\Gamma(t_f-\tau)} \left(1 - \tanh \left(\frac{de^{-2(t_f-\tau)}}{\Gamma(t_f-\tau)} \right) \right). \quad (32)$$

In Regime II, $t_f - \tau$ is of order one, and using the asymptotic form of the hyperbolic tangent one finds that

$$S_{\text{CFG}} - S_C \leq \frac{\sqrt{d}e^{-(t_f-\tau)}}{\Gamma(t_f-\tau)} \exp \left(-2 \frac{de^{-2(t_f-\tau)}}{\Gamma(t_f-\tau)} \right). \quad (33)$$

Therefore in Regime II the extra contribution to the score is exponentially small in d and its effect is completely negligible with respect to the one in Regime I.

Analysis of the CFG effect on the variance

Let us derive the equation for $\langle q^2(\tau) \rangle_\omega - \langle q(\tau) \rangle_\omega^2$.

Using Itô calculus, we have (multiplying by $q(\tau)$ in the equation for $\frac{dq(\tau)}{d\tau}$):

$$\begin{aligned} \frac{dq^2(\tau)}{d\tau} &= 2 + 2q^2(\tau) \left(1 - \frac{2}{\Gamma(t_f-\tau)} \right) + 2q(\tau) \frac{2\sqrt{d}}{\Gamma(t_f-\tau)} e^{-(t_f-\tau)} \\ &\quad + 2 \frac{2\omega\sqrt{d}}{\Gamma(t_f-\tau)} e^{-(t_f-\tau)} \left(q(\tau) - q(\tau) \tanh \left(\frac{q(\tau)\sqrt{d}e^{-(t_f-\tau)}}{\Gamma(t_f-\tau)} \right) \right) \\ &\quad + 2q(\tau)\eta(\tau). \end{aligned} \quad (34)$$

Taking the average and subtracting $2\langle q(\tau) \rangle_\omega \frac{d\langle q(\tau) \rangle_\omega}{d\tau}$, we find the equation for $\langle q^2(\tau) \rangle_\omega - \langle q(\tau) \rangle_\omega^2$:

$$\begin{aligned} \frac{d\langle q^2(\tau) \rangle_\omega - \langle q(\tau) \rangle_\omega^2}{d\tau} &= 2 + 2 \left(\langle q^2(\tau) \rangle_\omega - \langle q(\tau) \rangle_\omega^2 \right) \left(1 - \frac{2}{\Gamma(t_f-\tau)} \right) \\ &\quad + \omega \frac{4\sqrt{d}e^{-(t_f-\tau)}}{\Gamma(t_f-\tau)} \left(\langle q(\tau) \rangle_\omega \left\langle \tanh \left(\frac{q\sqrt{d}e^{-(t_f-\tau)}}{\Gamma(t_f-\tau)} \right) \right\rangle_\omega \right. \\ &\quad \left. - \langle q(\tau) \tanh \left(\frac{q\sqrt{d}e^{-(t_f-\tau)}}{\Gamma(t_f-\tau)} \right) \rangle_\omega \right). \end{aligned} \quad (35)$$

At the beginning of the backward process, one can expand $\tanh(x)$ and observe that the term in the parentheses is proportional to:

$$- \left(\langle q(\tau)^2 \rangle_\omega - \langle q(\tau) \rangle_\omega^2 \right), \quad (36)$$

which is negative. Therefore, we can conclude that the classifier-free-guidance-added term will result in shrinkage of the variance.

As for the mean, the main CFG effect on the variance is produced in Regime I, since the CFG score term is exponentially small in Regime II.

E Experimental details: Gaussian mixtures

In this section, we present experimental details for the numerical simulations involving Gaussian mixtures, describing the procedures and the hyperparameter configurations.

Numerical simulations. In the case of a mixture of two Gaussian clusters centered on $\pm\vec{m} \in \mathbb{R}^d$ with variance σ^2 , the score function reads as

$$S_{t_{CFG}}(\vec{x}(t), c) = -\frac{x(t)}{\Gamma_t} + \omega \frac{\vec{m}e^{-t}}{\Gamma_t} \left\{ c - \tanh\left(\frac{\vec{x}(t) \cdot \vec{m}e^{-t}}{\Gamma_t}\right) \right\} + \frac{c\vec{m}e^t}{\Gamma_t},$$

where $\Gamma_t = \Delta_t + \sigma^2 e^{-2t}$, with $\Delta_t = 1 - e^{-2t}$. We can then discretize the stochastic differential equation associated to the backward process as

$$\vec{x}(t+1) = \vec{x}(t) + \eta [\vec{x}(t) + 2S_{t_{CFG}}(\vec{x}(t), c)] + \vec{\eta}\sqrt{2\tau/L},$$

where $\vec{\eta} \sim \mathcal{N}(0, I)$, with $t_f = 8$ the time horizon and $t_f/L = 0.01$. We use $\vec{m} = [1, \dots, 1]$, $\sigma^2 = 1$, and each point is obtained by averaging over 100 initial conditions. The speciation time t_s is calculated as $t_s = -\frac{1}{2} \log d$. Throughout the experiments, we plot the evolution of $q(t) = \frac{\vec{x} \cdot \vec{m}}{|\vec{m}|}$, conditioning the guidance on the positive class with $c = 1$.

F Experimental details: Real-world analyses

F.1 Assets

In Table 2 we list the datasets and models used in our work along with their licensing.

Table 2 Assets used for our work.

Name	License/Link
COCO'14	https://www.cocodataset.org
ImageNet	https://www.image-net.org
CC12M	https://github.com/google-research-datasets/conceptual-12m
YFCC100M	https://www.multimediacommons.org
Florence-2	https://huggingface.co/microsoft/Florence-2-large/blob/main/LICENSE
DiT	https://github.com/facebookresearch/DiT/blob/main/LICENSE.txt
EDM2	https://github.com/NVlabs/edm2/blob/main/LICENSE.txt
MMDiT	https://github.com/lucidrains/mmdit/blob/main/LICENSE
MDTV2	https://github.com/sail-sg/MDT/blob/main/LICENSE

F.2 Performing the time reparameterization

In the second part of the paper, we evaluate the score of DiT models, in discrete time, as introduced by Peebles and Xie (2023). In this context, the forward process has a linear variance schedule $\{\beta_t'\}_{t'=1}^L$, where L is the time horizon given as a number of steps. Here, the variance evolves linearly from $\beta_1 = 10^{-4}$ to $\beta_{1000} = 2 \times 10^{-2}$. An unguided sample, at timestep t' , denoted $\vec{x}(t')$ can be expressed readily from its initial state, $\vec{x}(0) = \vec{a}$, as

$$\vec{x}(t') = \sqrt{\bar{\alpha}(t')} \vec{a} + \sqrt{1 - \bar{\alpha}(t')} \vec{\xi}(t')$$

where $\bar{\alpha}(t') = \prod_{s=1}^{t'} (1 - \beta_s)$ and $\vec{\xi}$ is standard Gaussian noise. This equation corresponds to the discretization of the Ornstein-Uhlenbeck Eq. (9) under the following timestep t' reparameterization,

$$t = -\frac{1}{2} \log(\bar{\alpha}(t')),$$

where time t is as defined in the main manuscript. This gives the map between our theoretical timescale used in Gaussian mixtures, and the one used in real-world settings. We note that, as the neural network predicts the noise, in order to calculate the score, one needs to normalize the output by the standard deviation (depending on the variance schedule). In this case, this corresponds to dividing the neural network output by $\sigma(t') = \sqrt{1 - \bar{\alpha}(t')}$. **In numerical experiments, we divide the CFG-added-term** by $\sigma(t') + 1$ to avoid numerical errors. This is theoretically justified due to the fact that, as discussed in main paper, the score difference $|S_{t'}(\vec{x}, c) - S_{t'}(\vec{x})|$ for large forward times decays exponentially (as $e^{-t'}$) to zero.

For completeness, we present the full comparison of numerical simulations to real-world using the time-reparameterization to plot the timesteps on the same time-scale. Our findings are portrayed in Figure 10. As each framework uses a separate time reparameterization, the x-axis needs to be recalculated accordingly. For the EDM2 framework (Karras et al., 2022), this can be done as follows: given a noise schedule $\sigma(t)$, the reparameterization can be calculated as $t'(t) = (1/2) \log(1 + \sigma^2(t))$, assuming that $s(t) = 1$. For the case $s(t)$, one needs to resort to equation Eq. (2).

F.3 Hyperparameter configurations

Here, we give exact hyperparameters used for reproducing all our experiments. The real-world experiments are performed using NVIDIA H100 Tensor Core - 80GB HBM3. The EDM2-S model has a model size of 280 Mparams and 102 Gflops, whereas the DiT-XL/2 model has model size of 675 Mparams and 525 Gflops. Parameter α is tuned in (0.3, 0.95) with an increment of 0.05 and parameter ω is tuned in (1., 12.) with an increment of 0.05. To tune ω , we first perform a small grid search of the increment of 1. and then do a further extensive search of the best performing ω_{prelim} in the range $(\omega_{prelim} - 2., \omega_{prelim} + 2.)$ with the 0.05 increment. We begin with the hyperparameters used in our figures.

In **Figure 1**, we plot the generation of images starting from 7 initial seeds for the DiT/XL-2 model trained on ImageNet-1K (256 × 256) for (1) conditional model without using guidance, (2) standard CFG with $\omega = 4.$, and Power-Law CFG with $\alpha = 0.9, \omega = 8.$

In **Figure 2**, the first two plots correspond to the histograms of the samples generated using the backward process with dimensions $d \in \{2, 200\}$ and guidance parameter $\omega \in \{0, 0.2, 15\}$, with $\sigma^2 = 1$, averaged over 10,000 trajectories. The last two plots correspond to the actual trajectories projected onto the target mean $+\vec{m}$ for values of $\omega \in \{0., 5., 10., 15., 20.\}$.

In **Figure 3**, we plot the evolution of the 1D backward dynamics with means at ± 4 and unit variance. The potential plotted corresponds to equation $V(q, t) = \frac{1}{2}q^2 - 2 \log \cosh(qe^{-(t-t_s)})$. For the derivation of this potential, see Appendix B.2 in Biroli et al. (2024).

In **left part** of **Figure 4**, we evaluate the difference of the conditional and unconditional score for Gaussian mixtures, $|S_t(x, c) - S_t(x)|$ for dimensions $d \in \{1, 5, 20, 50, 200\}$ with 2 classes, using $\omega = 5, \sigma^2 = 1$, averaged over 10,000 trajectories. For the **middle part**, we use $\omega = 5., d = 200$ and change the $\alpha \in \{-0.5, -0.3, -0.1, 0., 0.2, 0.5, 0.9\}$. The forward time in the equation goes from 0. to 8., which we denote as *sampling time* going from 0 (corresponding to data) to 1 (corresponding to noise) for simplicity of the exposition. In **right part**, we plot the score difference for four real-world models: DiT/XL-2, EDM2-S, MMDiT and MDTv2, all trained using the diffusion objective. As each of the models' default hyperparameters have different number of sampling steps, we normalize the x-axis from 0 to 1: e.g., DiT framework uses 250 sampling steps, EDM2 uses 32 and for the text-to-image models we use 50 sampling steps. The y-axis is normalized to be between 0 and 1 for easier readability. All hyperparameters are set to the default ones.

In **Figure 5**, we perform sensitivity analysis for EDM2-S trained on ImageNet-1K (512 × 512), taking α from 0. to 0.99 with 20 evenly spaced values, and ω from 1. to 10. with 20 evenly spaced values as well. The right plot involves α values of 0.2, 0.4, 0.6, 0.8, 0.9 with ω in the range of 1. to 12.5 with evenly spaced 20 points.

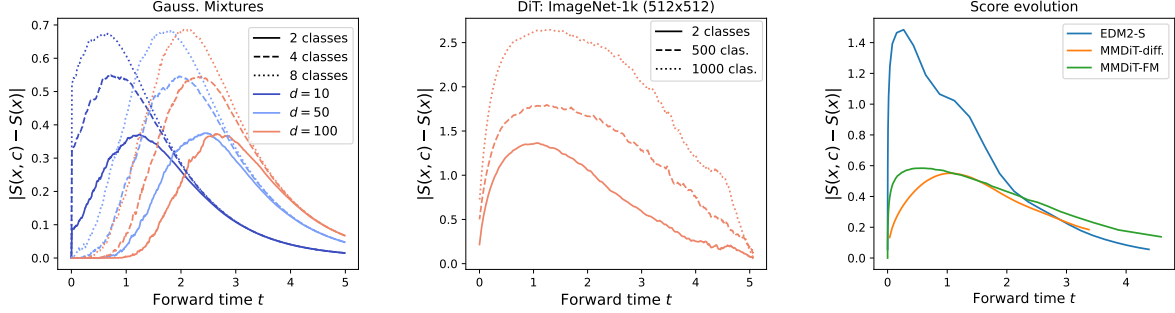


Figure 10 Evolution of the score differences for numerical simulations and real-world experiments projected onto the same time-scale for direct comparison. **First:** Numerically simulating mixture of two, four, and eight Gaussians with equidistant means on a sphere ($r = \sqrt{d}$), with varying dimension d , with $\omega = 4, \sigma^2 = 1$, averaged over 10,000 trajectories. As d increases, the score difference starts to increase at an earlier backward time τ . Additionally, as the number of classes increases, the magnitude of the score difference grows, as well as the duration of large difference between the scores. **Second:** Three DiT/XL-2 models trained on ImageNet-1K using 2, 500, and 1000 classes (image size 512×512). We observe a similar pattern: as d increases, the score difference becomes larger at an earlier time. Furthermore, as the number of classes increases, the magnitude of the score difference increases, together with the duration for which the difference remains large. **Third:** evolution of the remaining models used in our experiments (EDM2-S, MMDiT and MDTv2). We observe a similar behavior to theory and the DiT/XL-2 models.

In **Figure 6** we show generations of DiT/XL-2 trained on ImageNet-1K (256×256). The red panel contains generations from weak and strong standard CFG (corresponding to $\omega = 2$ and $\omega = 5$, respectively). The green panel corresponds to power-law CFG ($\alpha = 0.9$) with weak and strong guidance (corresponding to $\omega = 2$ and $\omega = 10$). The blue panel corresponds to combinations of α and ω (0, 2.5), (0.25, 4.), (0.5, 6.) and (0.9, 8.).

In **Figure 7**, we examine the following functions:

$$V_{\text{class}}(q, t; c) = \frac{1}{2}q^2 - ce^{-(t-t_s)}q + 2$$

$$V_{\text{extra}}(q, t; c) = -ce^{-(t-t_s)}q + \log\left(\cosh\left(qe^{-(t-t_s)}\right)\right) + \log(2),$$

where the plots correspond to V_{class} , V_{extr} and $(V_{\text{class}} + \omega V_{\text{extr}})$ with $\omega = 3$ respectively. We select $c = 1$, and fix the speciation time to $t_s = .5$. The additive constants are added for clarity only.

In **Figure 8**, we plot the backward diffusion in a Gaussian mixture model with $d = 16, \sigma^2 = 4, \omega = 8$. The CFG is either run at all times (top curve), stopped at times t_1 or not used at all (bottom curve).

In **Figure 9**, we perform linear CFG with $\omega = 8$ from $t = 5$ to $t = t_1$, after which we turn CFG off ($\omega = 0$) at times $t_1 = 0.69, 1.38, 3.19$.

In **Figure 10**, we use DiT/XL-2 model trained on 2, 500 and 1000 classes. For 2 classes, we have selected the same classes as in [Biroli et al. \(2024\)](#), and for the 500 classes we selected the first 500 classes in ImageNet-1K. The x-axis represents the Forward time t , where the parameterization is obtained as explained in [App. F.2](#).

In **Figures 26-27**, we perform the same experiment as in [Figure 10](#) and use $d = 16$ and $\sigma^2 = 4$.

Finally, in the **first column** of **Figure 28**, we plot the estimated Jensen-Shannon Divergence between the target samples corresponding to a randomly selected class and the diffusion particles throughout the backward trajectory. Note that this is performed in latent space. For obtaining the **middle column**, we first take all data samples from one class, embed them into the latent space and calculate the centroid corresponding to this class. Then, we normalize the centroid (making it unit norm) and plot the dot product of the particles throughout the backward diffusion process with the calculated centroid. The **right column** corresponds to the score difference. Across all experiments, we selected $\omega = 4$, sampled using DDPM ([Ho et al., 2020](#)) using 250 sampling steps, averaged over 25 samples. All other hyperparameter configurations are set to the default.

Table 3 displays the hyperparameters used to obtain the results given in [Table 1](#). The evaluation code relied on EvalGIM library by [Hall et al. \(2024\)](#).

Table 3 Hyperparameter configurations used throughout the experiments.

(α, ω)	DiT/XL-2	EDM2-S	Diff. MMDiT CC12m	Diff. MDTv2 IMN-1K	FM MMDiT COCO	FM MMDiT CC12M
Standard	(0., 1.5)	(0., 1.4)	(0., 1.55)	(0., 1, 2)	(0., 2.)	(0., 2.1)
Non-linear	(0.75, 4.85)	(0.85, 11.4)	(0.6, 7.0)	(0.8, 8.5)	(0.7, 10.15)	(0.6, 8.05)
Non-lin. + Limited	(0.8, 4.95)	(0.9, 12.05)	(0.55, 8.25)	(0.85, 8.25)	(0.75, 10.05)	(0.65, 7.85)
Non-lin. + CADs	(0.7, 4.75)	(0.80, 11.75)	(0.75, 8.15)	(0.80, 8.40)	(0.75, 10.75)	(0.55, 7.90)

F.4 Further results

Here, we detail the remaining experiments conducted. We provide the following:

- Diversity and coverage metrics corresponding to experiments in Table 1 (see Table 4)
- Ablation studies showing that Power-Law CFG outperforms standard linear CFG when changing the number of steps (see Tables 5-10)
- Sensitivity analysis showing the FID benefit for increasing value of α (see Section F.4.1, Figures 11-13)
- Further qualitative analyses of power-law CFG for either fixed ω and varying α or varying ω and varying α (see Sections F.4.2 and F.4.3)
- Further generation examples of DiT/XL-2 and MMDiT diffusion model (see Sections F.4.4 and F.4.5)

Diversity and coverage metrics. In Table 4 present additional quantitative evaluations of our method, focusing on diversity and coverage metrics (as described in Hall et al. (2024)), which complement the results shown in Table 1. Our analysis compares power-law CFG to standard CFG and state-of-the-art guidance methods, including combinations with CADs (Sadat et al., 2023) and limited-guidance (Kynkäänniemi et al., 2024), which proved to be the most competitive approaches. As demonstrated in the main manuscript, power-law CFG generally outperforms standard CFG (indicated by arrows in the table). Moreover, when combined with CADs and limited-interval guidance, it yields improved results over existing methods in many cases.

Ablation studies. In Tables 5 through 10, we conduct ablation studies on two class-conditional and four text-to-image models, demonstrating that non-linear power-law CFG consistently surpasses standard CFG across varying sampling steps. The results show improved FID performance and enhanced outcomes across multiple metrics when using the non-linear approach compared to standard CFG.

Sensitivity analysis. In Section F.4.1, we present additional sensitivity analyses that build on Section 5.3 and Figure 5, demonstrating that high values of α consistently enhance performance, improving robustness and stability during ω tuning. As noted in the main manuscript, while power-law CFG introduces an additional hyperparameter, α , extensive hyperparameter tuning was unnecessary, with large values like $\alpha = 0.9$ consistently performing well. This is evidenced in Section F.4.1, Figures 11 to 13, which show that higher α values reliably improve FID scores. Class-conditional models (Figure 11) exhibit greater benefits than text-to-image models (Figures 12 and 13), though both show improved performance with Power-Law CFG compared to standard CFG.

Further qualitative analyses. In Sections F.4.2 and F.4.3, we provide additional qualitative examples for DiT-XL/2. Specifically, we conduct two studies: one varying the guidance parameter ω with a fixed α , and another varying α with a fixed ω . When α is fixed, increasing ω can lead to issues such as complete mode collapse (e.g., for the *jellyfish* class), oversaturation (e.g., for the *bee* class), or a significant loss of diversity (e.g., for the *dung beetle* class), which are common artifacts of standard classifier-free guidance. These effects are mitigated when using a non-linear power-law guidance approach. The second study explores the impact of increasing α while keeping ω constant, demonstrating enhanced diversity as α strength increases.

Further generation examples. In Sections F.4.4 and F.4.5, we present additional generation examples for class-conditional (DiT/XL-2) and text-to-image (MMDiT) models, demonstrating how power-law CFG enhances image details, thereby improving image quality and fidelity for individual images, and increases diversity when examining a set of images for a specific class.

Table 4 Comparison of EDM2-S on ImageNet-1K 512x512 data, Diffusion trained text-to-image MMDiT on CC12m data, and Flow-matching trained text-to-image MMDiT on COCO data. **Bolded** are the best results and underlined are the second best.

Model	EDM2-S (CC, IM-1K 512)		DiT/XL-2 (CC, IM-1K 256)		Diff. MMDiT (T2IM, CC12m)		FM MMDiT (T2IM, COCO)	
	Density	Coverage	Density	Coverage	Density	Coverage	Density	Coverage
Standard (Ho and Salimans, 2022)	0.850	0.764	0.951	0.801	1.091	0.840	0.902	0.772
Scheduler (Wang et al., 2024)	0.867	<u>0.780</u>	<u>1.117</u>	0.790	1.266	0.860	0.908	0.795
Limited (Kynkäänniemi et al., 2024)	0.845	0.777	1.130	0.840	1.258	0.857	0.915	0.808
Cosine (Gao et al., 2023)	0.850	0.769	1.102	0.822	1.106	0.840	0.920	0.802
CADS (Sadat et al., 2023)	0.854	0.765	0.999	0.853	1.222	0.860	<u>0.923</u>	0.779
APG (Sadat et al., 2024)	0.845	0.760	1.033	<u>0.867</u>	1.095	0.858	0.915	0.797
REG (Xia et al., 2024)	0.850	0.771	1.112	0.833	1.091	0.855	0.903	0.783
CFG++ (Chung et al., 2024)	N/A	N/A	N/A	N/A	1.265	0.859	0.919	0.784
Power-law CFG (Ours)	0.845 (↓)	0.760 (↑)	0.986 (↑)	0.844 (↑)	1.128 (↑)	0.850 (↑)	0.918 (↑)	0.778 (↑)
Power-law CFG + Limited (Ours)	0.850 (↑)	0.778 (↑)	1.115 (↓)	0.835 (↓)	1.286 (↑)	<u>0.860</u> (↑)	0.920 (↑)	0.795 (↓)
Power-law CFG + CADS (Ours)	<u>0.862</u> (↑)	0.782 (↑)	1.071 (↑)	0.876 (↑)	<u>1.279</u> (↑)	0.862 (↑)	0.924 (↑)	<u>0.804</u> (↑)

Table 5 Ablation study: Changing the number of sampling steps for Class-conditional: DiT ImageNet-1K 256x256

Version	Num. steps	α	ω	FID (↓)	IS (↑)	Precision (↑)	Recall (↑)	sFID (↓)
Stand. CFG	50	0	1.5	3.33	259.88	0.8163	0.5474	7.406
	100	0	1.4	2.64	233.72	0.8027	0.5831	5.720
	150	0	1.3	2.38	233.52	0.8032	0.5936	5.462
	200	0	1.35	2.29	234.92	0.8031	0.5950	5.331
	250	0	1.5	2.27	278.30	0.8291	0.5840	4.601
Non-lin. CFG	50	0.6	4.35	3.03	284.55	0.8215	0.5757	7.110
	100	0.6	3.4	2.32	274.36	0.8199	0.6012	5.432
	150	0.6	3.4	2.19	274.39	0.8202	0.6071	5.512
	200	0.75	4.8	2.17	276.98	0.8204	0.5956	5.567
	250	0.75	4.85	2.05	279.90	0.8310	0.5950	4.670

Table 6 Ablation study: Changing the number of sampling steps for Class-conditional: EDM2-S ImageNet-1K 512x512

Version	Num. Steps	α	ω	FID (↓)	α	ω	FID _{DINO} (↓)
Stand. CFG	8	0	1.95	4.78	0	2.3	103.33
	16	0	1.50	2.52	0	2.3	57.47
	32	0	1.40	2.29	0	2.3	54.78
	64	0	1.50	2.25	0	2.15	54.39
Non-lin. CFG	8	0.05	2.30	4.74	-0.25	1.5	100.81
	16	0.25	2.30	2.32	-0.05	2.15	56.92
	32	0.85	11.40	1.93	0.35	2.5	52.77
	64	0.85	11.30	1.89	0.35	2.1	52.56

Table 7 Ablation study: Changing the number of sampling steps for Diffusion text-to-image: MMDiT CC12m

Version	Num. Steps	α	ω	FID (\downarrow)	Clip score (\uparrow)	Coverage (\uparrow)	Density (\uparrow)	Precision (\uparrow)	Recall (\uparrow)
Stand. CFG	20	0	1.75	8.98	22.581	0.8392	1.104	0.6623	0.5545
	35	0	1.75	8.79	22.532	0.8450	1.124	0.6717	0.5590
	50	0	1.55	8.58	22.111	0.8401	1.109	0.6612	0.5692
	100	0	1.75	8.38	22.298	0.8462	1.117	0.6765	0.5698
Non-lin. CFG	20	0.25	3.05	8.94	22.773	0.8424	1.114	0.6619	0.5495
	35	0.65	7.5	8.40	22.590	0.8491	1.126	0.6638	0.5582
	50	0.60	7.0	8.11	22.415	0.8503	1.128	0.6703	0.5532
	100	0.75	9.5	8.02	22.563	0.8472	1.115	0.6747	0.5723

Table 8 Ablation study: Changing the number of sampling steps for Diffusion text-to-image: MDV2 ImageNet-1K 512x512

Version	Num. Steps	α	ω	FID (\downarrow)	Clip score (\uparrow)	Coverage (\uparrow)	Density (\uparrow)	Precision (\uparrow)	Recall (\uparrow)
Stand. CFG	20	0	1.55	5.30	23.949	0.8218	1.167	0.7475	0.5133
	30	0	1.55	4.09	23.998	0.8292	1.233	0.7492	0.5264
	40	0	1.6	3.85	24.011	0.8311	1.178	0.7602	0.5294
	50	0	1.2	3.68	24.306	0.8318	1.150	0.7510	0.5989
Non-lin. CFG	20	0.6	6.0	4.88	24.154	0.8251	1.236	0.7503	0.4916
	30	0.6	6.0	4.03	24.033	0.8344	1.205	0.7583	0.5332
	40	0.7	7.0	3.73	23.367	0.8353	1.181	0.7557	0.5546
	50	0.8	8.5	3.57	25.339	0.8361	1.170	0.7513	0.5609

Table 9 Ablation study: Changing the number of sampling steps for Flow-Matching text-to-image: MMDiT on COCO

Version	Num. Steps	α	ω	FID (\downarrow)	Clip score (\uparrow)	Coverage (\uparrow)	Density (\uparrow)	Precision (\uparrow)	Recall (\uparrow)
Stand. CFG	20	0	2.85	6.84	26.373	0.7529	0.8820	0.6121	0.5604
	30	0	1.95	5.84	25.948	0.7581	0.8668	0.6051	0.5879
	40	0	2.05	5.62	25.817	0.7651	0.8798	0.6091	0.5978
	50	0	2.00	5.20	25.714	0.7726	0.9026	0.6299	0.5940
Non-lin. CFG	20	0.5	9.75	6.47	25.981	0.7241	0.7762	0.5719	0.5851
	30	0.5	9.45	5.62	26.003	0.7577	0.8457	0.6105	0.5874
	40	0.6	9.05	5.45	25.113	0.7633	0.8549	0.6149	0.6030
	50	0.7	10.15	4.81	25.848	0.7782	0.9183	0.6208	0.6191

Table 10 Ablation study: Changing the number of sampling steps for Flow-Matching text-to-image: MMDiT on CC12m

Version	Num. Steps	α	ω	FID (\downarrow)	Clip score (\uparrow)	Coverage (\uparrow)	Density (\uparrow)	Precision (\uparrow)	Recall (\uparrow)
Stand. CFG	20	0	2.75	10.75	25.224	0.8289	1.069	0.6396	0.5803
	30	0	1.95	9.85	24.935	0.8318	1.068	0.6946	0.6000
	40	0	2.0	9.50	25.018	0.8461	1.103	0.7064	0.5907
	50	0	2.1	9.46	25.133	0.8520	1.145	0.7159	0.5946
Non-lin. CFG	20	0.2	3.25	10.68	25.585	0.8301	1.075	0.7101	0.5815
	30	0.5	10.0	9.81	25.002	0.8338	1.085	0.6968	0.5909
	40	0.6	9.35	9.17	24.794	0.8352	1.087	0.6909	0.6030
	50	0.6	8.05	9.00	24.723	0.8397	1.087	0.6911	0.6023

F.4.1 Sensitivity analysis

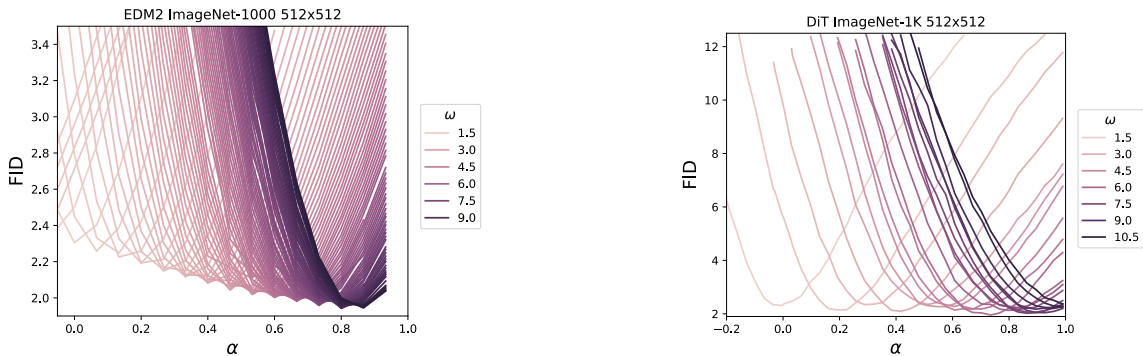


Figure 11 Class-conditional diffusion: image quality benefits from non-linear scheme, yielding lower FID for larger values of α .

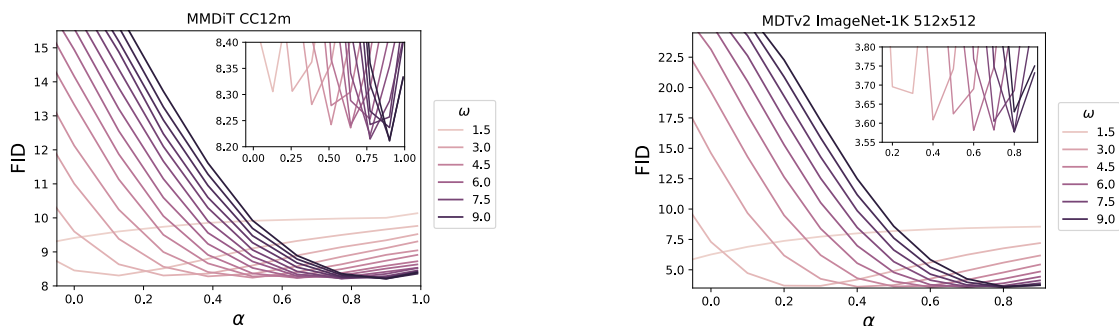


Figure 12 Text-to-image diffusion models: image quality benefits from non-linear scheme, yielding lower FID for larger values of α .

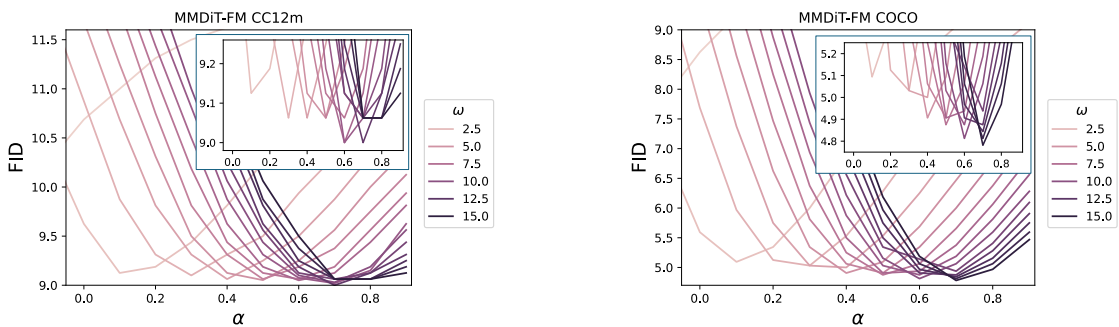
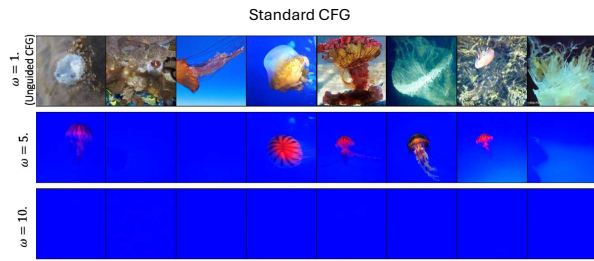
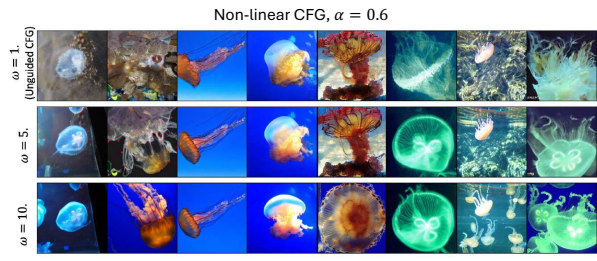


Figure 13 Text-to-image flow matching: image quality benefits from non-linear scheme, yielding lower FID for larger values of α .

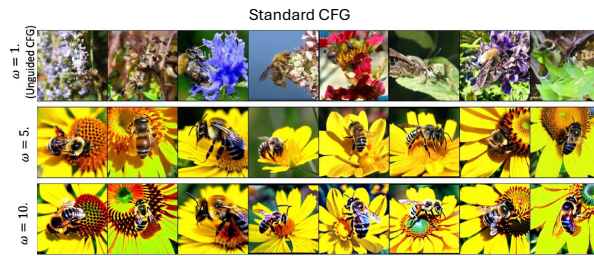
F.4.2 Qualitative analysis: varying ω , fixed α .



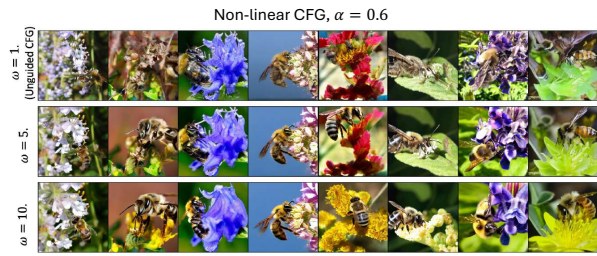
(a) Class 107: *jellyfish* with $\alpha = 0$.



(b) Class 107: *jellyfish* with $\alpha = 0.9$



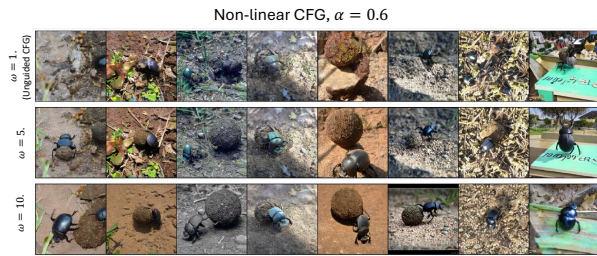
(c) Class 309: *bee* with $\alpha = 0$.



(d) Class 309: *bee* with $\alpha = 0.9$



(e) Class 305: *dung beetle* with $\alpha = 0$.



(f) Class 305: *dung beetle* with $\alpha = 0.9$

Figure 14 Generated images for different classes with varying values of ω and α . Each panel shows the effect of changing α from 0 to 0.9, demonstrating the impact on diversity and image quality.

F.4.3 Qualitative analysis: fixed ω , varying α .

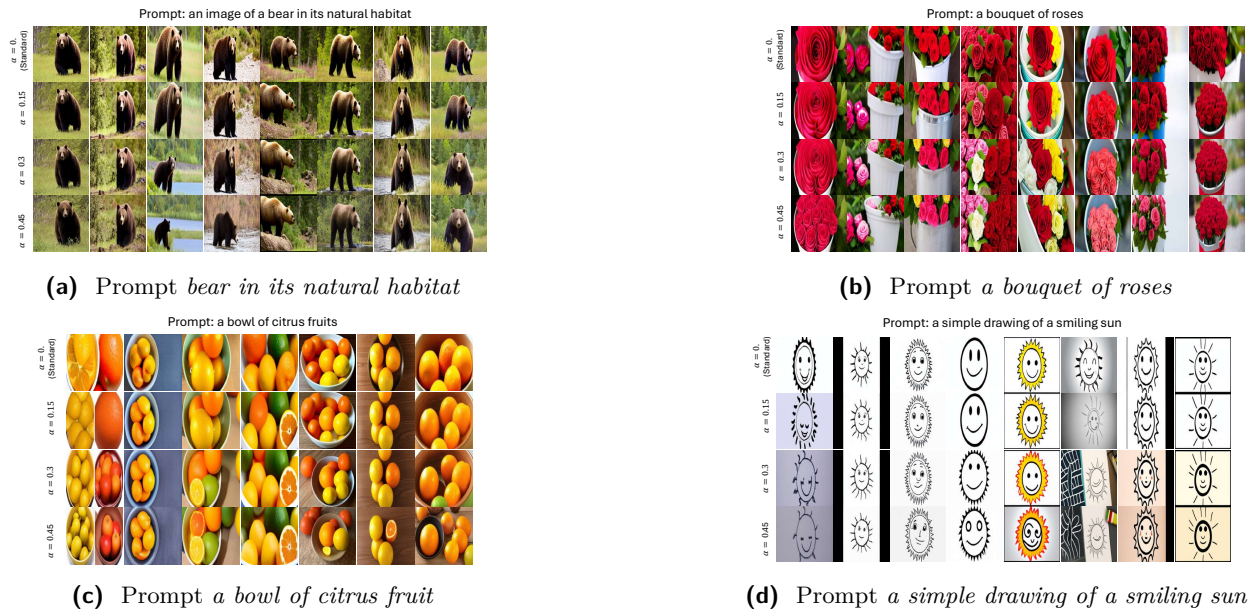


Figure 15 T2IM generated images for different prompts with $\omega = 4$, and varying value of α .

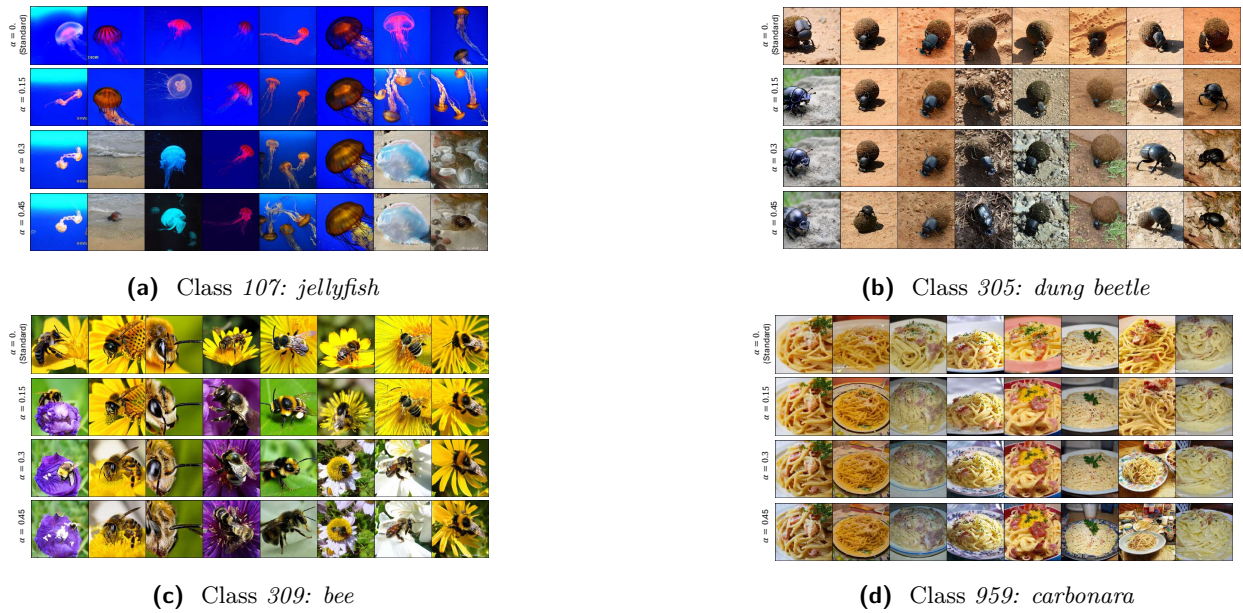


Figure 16 CC generated images for different classes with $\omega = 4$, and varying value of α .

F.4.4 Generated Images by DiT/XL-2 (256x256)

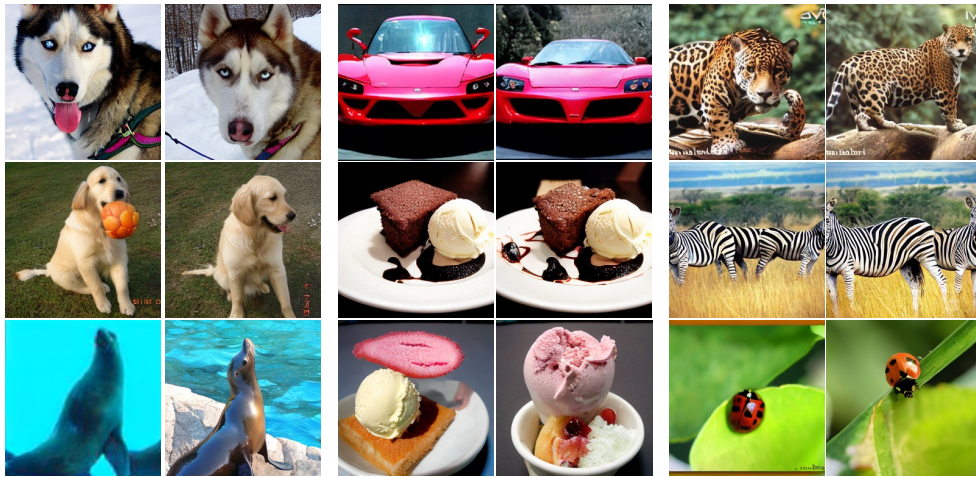


Figure 17 Additional examples generated by DiT/XL-2 using Standard CFG ($\omega = 4$) and Power-Law CFG ($\omega = 8, \alpha = 0.7$). Image pairs start from the same noise (same seed). The resulting pairs represent Standard CFG on the left and Power-Law CFG on the right.



Figure 18 Gen. images conditioned on the class *pineapple* with Standard CFG ($\omega = 4$).



Figure 19 Gen. images conditioned on class *pineapple* with Power-Law CFG ($\omega = 8, \alpha = 0.7$).



Figure 20 Gen. images conditioned on the class *water ouzel, dipper* using Standard CFG with $\omega = 4$.



Figure 21 Gen. images conditioned on the class *water ouzel, dipper* using Power-Law CFG with $\omega = 8$, $\alpha = 0.7$.



Figure 22 Gen. images conditioned on the class *vine snake* using Standard CFG with $\omega = 4$.



Figure 23 Gen. images conditioned on the class *vine snake* using Power-Law CFG with $\omega = 8$, $\alpha = 0.7$.

F.4.5 Generated Images by MMDiT model (diffusion objective, resolution 512x512)



Figure 24 Images generated conditioned on the textual prompt *Glowing mushrooms in a dark forest*. using Standard CFG with $\omega = 3$ (top two rows) and Power-Law CFG with $\omega = 10, \alpha = 0.8$ (bottom two rows).

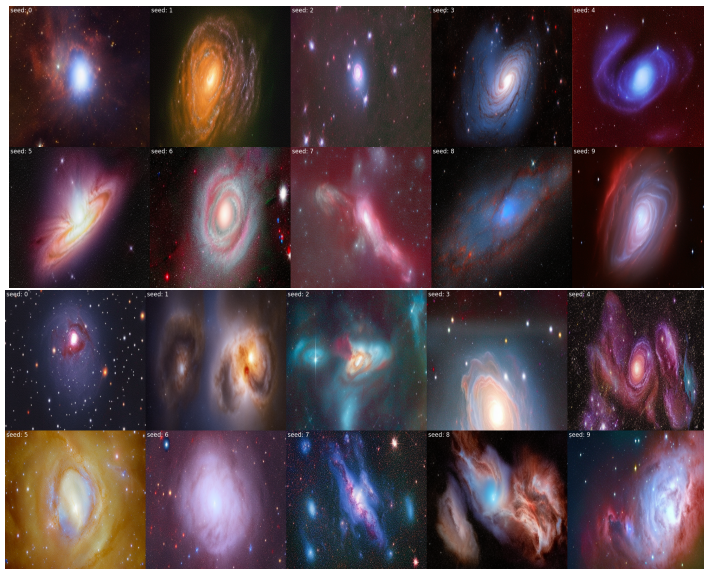


Figure 25 Images generated conditioned on the textual prompt *Stunning, breathtaking view of a galaxy or nebula* using Standard CFG ($\omega = 3$, top two rows) and Power-Law CFG ($\omega = 10, \alpha = 0.8$, bottom two rows).

G Further notes on non-linear CFG

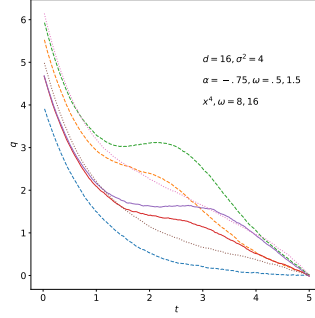


Figure 26 $\langle q \rangle$ versus time in Gaussian mixture with $d = 16$ and $\sigma^2 = 4$. The dashed lines are obtained with standard CFG with $\omega = 0, 8, 16$ from bottom to top. The dotted lines are obtained with the Power-Law scheme $f(x) = \omega x^{-.75}$ with $\omega = .5, 1.5$ from bottom to top. The full lines are obtained with the non-linear guidance of Eq.(38) with $\gamma = 4$ and $\omega = 8, 16$ from bottom to top. The Rescaled Power-law non-linear scheme departs from $q = 0$ at large time on a trajectory similar to the linear scheme and to the Power-Law non-linear scheme. But it gives a smaller bias at $t = 0$.

The first non-linear CFG proposal, the power-law CFG with $\phi_t(s) = \omega s^\alpha$ and $\alpha > -1$ results in the following guidance scheme:

$$\vec{S}_t^{\text{PL}}(\vec{x}, c) = S_t(\vec{x}, c) + \omega [S_t(\vec{x}, c) - S_t(\vec{x})] \left| \vec{S}_t(\vec{x}, c) - \vec{S}_t(\vec{x}) \right|^\alpha. \quad (37)$$

As mentioned, the ℓ_2 distance between scores $\delta S_t = |\vec{S}_t(\vec{x}, c) - \vec{S}_t(\vec{x})|$ is exponentially small both at the beginning of the backward process (as both conditional and unconditional distributions are standard Gaussian clouds) and before exiting Regime I (as shown in Section 4), after which it remains zero. This non-linear scheme automatically switches off in Regime II and has the following properties: choosing $\alpha < 0$ provides guidance which speeds up convergence to the target at early times, while $\alpha > 0$ dampens the guidance for small δS_t and strengthens it for large δS_t . In practice, we found positive values for α to perform best. In numerical experiments for finite dimension it biases the distribution obtained at $t = 0$ (see Fig.28).

One would like to have different non-linearities applying to the regimes $t \gg t_s$ and $t < t_s$. One possibility is to use the following version, which extends to more general effective distributions $P_0(\vec{a})e^{-\vec{a}^2 s(t)/(2s(t)^2 \sigma(t)^2)}$ with non-standard $s(t)$ and $\sigma(t)$.

Rescaled Power-law CFG. Here, by denoting with $\langle \cdot \rangle$ the expectation w.r.t. the effective distribution $P_0(\vec{a})e^{-\vec{a}^2 s(t)/(2s(t)^2 \sigma(t)^2)}$, the score difference can be expressed as $|\vec{S}_t(\vec{x}, c) - \vec{S}_t(\vec{x})| = (1/(s(t)\sigma(t)^2)) |\langle \vec{a} \rangle_{\vec{x}, c} - \langle \vec{a} \rangle_{\vec{x}}|$, where $s(t)$ and $\sigma(t)$ are related to the functions $f(t)$ and $g(t)$ by $s(t) = \exp \int_0^t d\tau f(\tau)$ and $\sigma(t) = \int_0^t d\tau g(\tau)^2 / s(\tau)^2$. Therefore the non-linear function depends on the difference between the estimators of the initial value \vec{a} , given $\vec{x}(t)$, in the class and in the full distribution. This difference is typically a function that decreases with the time of the backward process. This suggests to use a non-linear CFG of the form

$$\begin{aligned} \vec{S}_t^{\text{RPL}}(\vec{x}, c) &= \vec{S}_t(\vec{x}, c) + \omega \left[\vec{S}_t(\vec{x}, c) - \vec{S}_t(\vec{x}) \right] |\langle \vec{a} \rangle_{\vec{x}, c} - \langle \vec{a} \rangle_{\vec{x}}|^\gamma \\ &= \vec{S}_t(\vec{x}, c) + \omega \left[\vec{S}_t(\vec{x}, c) - \vec{S}_t(\vec{x}) \right] \left| \vec{S}_t(\vec{x}, c) - \vec{S}_t(\vec{x}) \right|^\gamma s(t)^\gamma \sigma(t)^{2\gamma}, \end{aligned} \quad (38)$$

with positive γ . As we will show in Figures 26-27, this non-linear guidance term has interesting performance in terms of combining a rapid drift toward the desired class c at early stages of the backward process together with small bias in the finite distribution in finite dimensional problems.

The behavior of both versions is portrayed in Figure 28: both non-lin. versions yield smaller bias at $t = 0$. Furthermore, Figure 28 also displays additional experiments highlighting the benefits of non-linear versions.

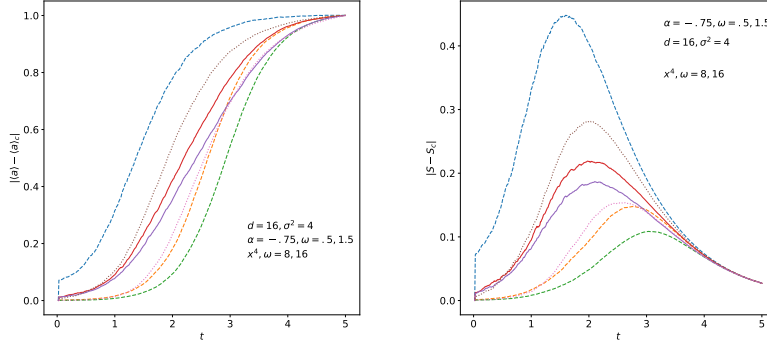


Figure 27 We perform the same experiment as in Fig. 26. Left: the value of $|\langle \vec{a} \rangle_{\vec{x}=\vec{0},c} - \langle \vec{a} \rangle_{\vec{x}=\vec{0}}|$. Right: the value of $|S_t(\vec{x}, a) - S_t(\vec{x})|$, with the same linestyle and color code as in Fig. 26.

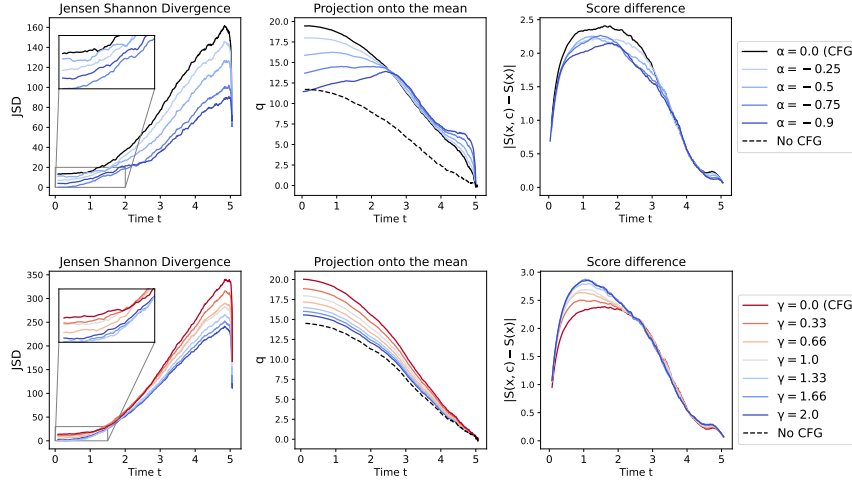


Figure 28 Real-world experiments using DiT/XL-2 (Peebles and Xie, 2023) trained on ImageNet-1000 (Deng et al., 2009): randomly selected class with $\omega = 4$, using DDPM (Ho et al., 2020) with 250 sampling steps, averaged over 25 samples. **First column:** Power-Law CFG. **Second column:** Rescaled Power-Law CFG (38). **Left column:** Jensen-Shannon Divergence between the embedded data points corresponding to randomly selected class and the generated samples as a function of reverse time τ . **Middle column:** mean dot product of the normalized class centroid and the diff. trajectories $\vec{x} \cdot \vec{c}_i / \|\vec{c}_i\|$ (in latent space) as a function of reverse time τ . **Right column:** Evolution of the distance between cond. and uncond. scores. From all three plots, we can see that using first (second) version of non-linear CFG with $\alpha < 0$ ($\gamma > 0$) results in paths that have smaller JSD, estimated as in Wang et al. (2009), throughout the whole trajectory and smaller overshoot of the distribution’s mean at $\tau = 0$. We can also see that the score difference $|S_\tau(x, c) - S_\tau(x)|$ has the same qualitative behavior as in numerical simulations of Gaussian mixtures.

H Impact Statement

This study contributes to the growing body of research aimed at deepening our theoretical understanding of diffusion models and their broader implications for generative modeling. By bridging the gap between theory and practice, we strive to improve the performance and efficiency of these models, which have far-reaching applications in various fields.

However, as with any powerful technology, there are also potential risks associated with development and deployment of advanced generative models. The increasing sophistication of deepfakes raises concerns about misinformation, propaganda, and the erosion of trust in digital media. Moreover, the misuse of generative models for malicious purposes, such as creating fake identities or spreading disinformation, poses significant threats to individuals, communities, and society as a whole.

In light of these challenges, we hope that our paper, along with many others that aim to improve understanding of the models, will contribute to a deeper understanding of their strengths and limitations. We believe it is essential for developing effective strategies to mitigate the risks associated with generative models, and we hope that our work will be a step toward achieving this goal.